



Provided by the author(s) and University of Galway in accordance with publisher policies. Please cite the published version when available.

Title	In situ <sup>10</sup> Be production-rate calibration from a <sup>14</sup> C-dated late-glacial moraine belt in Rannoch Moor, central Scottish Highlands
Author(s)	Putnam, Aaron E.; Bromley, Gordon R.M.; Rademaker, Kurt; Schaefer, Joerg M.
Publication Date	2018-11-23
Publication Information	Putnam, Aaron E., Bromley, Gordon R. M., Rademaker, Kurt, & Schaefer, Joerg M. (2019). In situ <sup>10</sup> Be production-rate calibration from a <sup>14</sup> C-dated late-glacial moraine belt in Rannoch Moor, central Scottish Highlands. <i>Quaternary Geochronology</i> , 50, 109-125. doi: <a href="https://doi.org/10.1016/j.quageo.2018.11.006">https://doi.org/10.1016/j.quageo.2018.11.006</a>
Publisher	Elsevier
Link to publisher's version	<a href="https://doi.org/10.1016/j.quageo.2018.11.006">https://doi.org/10.1016/j.quageo.2018.11.006</a>
Item record	<a href="http://hdl.handle.net/10379/14774">http://hdl.handle.net/10379/14774</a>
DOI	<a href="http://dx.doi.org/10.1016/j.quageo.2018.11.006">http://dx.doi.org/10.1016/j.quageo.2018.11.006</a>

Downloaded 2024-04-26T20:12:35Z

Some rights reserved. For more information, please see the item record link above.



1 An *in situ*  $^{10}\text{Be}$  production-rate calibration from a  $^{14}\text{C}$ -dated late-glacial moraine belt in Rannoch  
2 Moor, central Scottish Highlands

3

4 Aaron E. Putnam<sup>1,2</sup>, Gordon R. M. Bromley<sup>3</sup>, Kurt Rademaker<sup>4</sup>, Joerg M. Schaefer<sup>2</sup>

5

6 <sup>1</sup>School of Earth and Climate Sciences and Climate Change Institute, University of Maine,

7 Orono, ME 04473, USA

8 <sup>2</sup>Lamont-Doherty Earth Observatory and Department of Earth and Environmental Sciences,

9 Columbia University, Palisades, NY 10964, USA

10 <sup>3</sup>School of Geography and Archaeology and Ryan Institute, National University of Ireland,

11 Galway, Ireland

12 <sup>4</sup>Department of Anthropology, Michigan State University, East Lansing, MI 48824, USA

13

14

15 Highlights:

16 - We present a  $^{10}\text{Be}$  production-rate calibration data set for the central Scottish Highlands.

17 - Calibration landform chronology is constrained by bracketing  $^{14}\text{C}$  ages.

18 - Results agree with other distal calibration data from independently dated landforms.

19 - Results are at odds with Scottish calibrations based on indirectly dated landforms.

20

21 Keywords: Cosmogenic nuclide, moraine, Younger Dryas, radiocarbon

22

23 Abstract

24

25 An objective of terrestrial *in situ* cosmogenic nuclide research is to obtain precise and accurate  
26 production-rate estimates on the basis of geological calibration sites from a diverse range of  
27 latitudes and altitudes. However, a challenge has been to establish production rates on the  
28 basis of landforms for which independent ages have been determined directly using absolute  
29 isotopic dating techniques. Here we present a  $^{10}\text{Be}$  production-rate calibration (for neutron  
30 spallation) from a recessional moraine belt located in Rannoch Moor, central Scottish Highlands  
31 ( $56.63^\circ\text{N}$ ,  $4.77^\circ\text{W}$ ;  $\sim 310\text{--}330$  m a.s.l.). This moraine belt was deposited at the margin of the  
32 disintegrating late-glacial West Highland ice field (WHIF) during the final stages of deglaciation.  
33 Minimum-limiting  $^{14}\text{C}$  dates on macrofossils of the earliest terrestrial vegetation to arrive on  
34 the landscape place the timing of moraine abandonment, and hence exposure of morainal  
35 boulder surfaces to the cosmic-ray flux, to no later than  $12,480 \pm 100$  calendar years before C.E.  
36 1950 (cal yrs BP). Maximum-limiting  $^{14}\text{C}$  dates on marine shells incorporated into basal tills  
37 deposited during expansion of the WHIF to its full late-glacial extent place the onset of  
38 deglaciation, and thus deglaciation of Rannoch Moor, to no earlier than  $12,700 \pm 100$  cal yrs BP.  
39 After removal of a single high-concentration outlier, surface  $^{10}\text{Be}$  concentrations of 11 boulders  
40 rooted in two sub-parallel moraine ridges exhibit a high degree of internal consistency and an  
41 arithmetic mean of  $6.93 \pm 0.24$  [ $\times 10^4$ ] atoms  $\text{g}^{-1}$  ( $1\sigma$ ). This data set yields a site-specific  $^{10}\text{Be}$   
42 production rate of  $5.50 \pm 0.18$  at  $\text{g}^{-1} \text{yr}^{-1}$ , based on the midpoint age  $12,590 \pm 140$  cal yrs BP of  
43 the bracketing  $^{14}\text{C}$  chronology. Transforming this result to sea-level/high-latitude (SLHL)  
44 neutron-spallation  $^{10}\text{Be}$  production-rate values using Version 3 of the University of Washington

45 (UW) Online Production-Rate Calculator yields upper and lower bounds, and a mid-point rate.  
46 Maximum-limiting SLHL  $^{10}\text{Be}$  production rates, based on minimum-limiting  $^{14}\text{C}$  age control, are  
47  $3.95 \pm 0.11$  (2.7%) at  $\text{g}^{-1}\text{yr}^{-1}$  for the commonly used 'Lm' and 'St' scaling protocols. The  
48 corresponding (non-dimensional) correction factor for a reference production rate determined  
49 by the LSDn scaling model is  $0.79 \pm 0.02$  (2.7%). Minimum-limiting SLHL reference  $^{10}\text{Be}$   
50 production rates, based on maximum-limiting  $^{14}\text{C}$  age control, are  $3.88 \pm 0.11$  (2.7%) at  $\text{g}^{-1}\text{yr}^{-1}$   
51 (St) and  $3.89 \pm 0.11$  (2.7%) at  $\text{g}^{-1}\text{yr}^{-1}$  (Lm). The corresponding correction factor for LSDn scaling is  
52  $0.77 \pm 0.02$  (2.7%). SLHL reference production-rate values based on a midpoint age of  $12,590 \pm$   
53  $140$  yrs are  $3.91 \pm 0.11$  (2.8%) at  $\text{g}^{-1}\text{yr}^{-1}$  (St) and  $3.92 \pm 0.11$  (2.8%) at  $\text{g}^{-1}\text{yr}^{-1}$  (Lm). The  
54 corresponding correction factor for LSDn scaling is  $0.78 \pm 0.02$ . The production-rate calibration  
55 data set presented here for Scotland yields SLHL values that agree with those determined from  
56 calibration data sets based on directly dated landforms from northeastern North America, the  
57 Arctic, the Swiss Alps, the Southern Hemisphere middle latitudes, and from the high tropical  
58 Andes. We suggest that this production-rate calibration data set from the central Scottish  
59 Highlands, used together with the UW online calculators, will produce accurate  $^{10}\text{Be}$  surface-  
60 exposure ages in the British Isles.

61

62

63 1. Introduction

64           Knowing the rates at which cosmogenic nuclides are produced *in situ* beneath exposed  
65 rock surfaces is essential for the calculation of surface-exposure ages and erosion rates used in  
66 studies of landform chronologies and Earth-surface processes. A challenge remains to improve  
67 the precision and accuracy of cosmogenic nuclide production rates for the purpose of  
68 developing more accurate surface-exposure chronologies. A leading approach has been to  
69 determine production rates empirically by targeting geological calibration sites in which  
70 cosmogenic nuclide concentrations can be measured *in situ* from rock surfaces associated with  
71 landforms of independently known age (e.g., Balco et al., 2009; Balco et al., 2008; Borchers et  
72 al., 2016; Goehring et al., 2010). Empirically determined site-specific production rates are then  
73 scaled to other locations using models that account for spatial changes in nuclide production  
74 with atmospheric pressure, geomagnetic latitude (Lal, 1991; Stone, 2000), and, in some cases,  
75 temporal variations in the strength of Earth’s magnetic field and solar wind (Balco et al., 2008;  
76 Borchers et al., 2016; Lifton et al., 2005; Lifton et al., 2014; Lifton et al., 2008; Pigati and Lifton,  
77 2004). Production rates have been conventionally scaled to a nominal value at sea-level and  
78 high latitude (SLHL) in order to facilitate comparison among calibration sites in disparate  
79 locations (Balco, 2011; Balco et al., 2009; Balco et al., 2008; Borchers et al., 2016; Goehring et  
80 al., 2010; Kaplan et al., 2011; Putnam et al., 2010b). A community-wide effort devoted to  
81 developing a network of geological calibration sites, distributed across diverse latitudes and  
82 altitudes, has improved understanding of cosmogenic nuclide production rates on a global basis  
83 and has in turn helped to hone scaling methods (Balco et al., 2008; Borchers et al., 2016;  
84 Heyman, 2014; Phillips, 2015; Phillips et al., 2016).

85           There is particular interest in constraining *in situ*  $^{10}\text{Be}$  spallation production rates and  
86 scaling protocols. Because of the comparatively uncomplicated production systematics of this  
87 relatively long-lived nuclide [e.g., half-life = 1.4 Myrs (Chmeleff et al., 2010; Korschinek et al.,  
88 2009; Nishiizumi et al., 2007)] in the abundant mineral quartz,  $^{10}\text{Be}$  has become a commonly  
89 used geochronological tool. Improvements in the precision of  $^{10}\text{Be}$  analyses has led to  
90 transformational progress in the development of landform chronologies (Balco, 2011).  
91 Challenges remain, however, especially as answers to emerging scientific questions demand  
92 ever-greater chronological accuracy. For example, dispersion among existing SLHL  $^{10}\text{Be}$   
93 production-rate estimates indicates remaining uncertainties attending the geological calibration  
94 sites themselves and lingering imperfections in scaling models (Borchers et al., 2016; Phillips et  
95 al., 2016). This dispersion serves as a source of systematic uncertainty for landform  
96 chronologies, especially for regions with no nearby calibration sites. Furthermore, of the  
97 available published geological  $^{10}\text{Be}$  calibration sites, relatively few are anchored by landforms  
98 underpinned directly, at the site, by absolute chronologies. Many sites instead depend upon  
99 indirect associations among target landforms and other distal paleoclimatic/stratigraphic  
100 signatures (e.g., Ballantyne and Stone, 2012; Borchers et al., 2016; Goehring et al., 2012; Small  
101 and Fabel, 2015; Stroeven et al., 2015). Any incorrect assumptions incorporated into  
102 production-rates calibrated in this way could accidentally mislead attempts at evaluating and  
103 improving scaling protocols (Phillips et al., 2016). Further development of geological  $^{10}\text{Be}$   
104 production-rate calibration sites based upon landforms with direct and absolute-dated  
105 chronological constraints will help to sharpen empirical estimates of cosmogenic nuclide  
106 production rates and aid in improving scaling protocols.

107           Here, we present a  $^{10}\text{Be}$  production-rate calibration data set based on a  $^{14}\text{C}$ -dated late-  
108 glacial moraine belt located at Rannoch Moor, central Scottish Highlands. Although there are  
109 now four published  $^{10}\text{Be}$  production-rate calibration sites in Scotland (e.g., Ballantyne and  
110 Stone, 2012; Borchers et al., 2016; Small and Fabel, 2015), none is based on landforms that  
111 have been directly dated with absolute radiometric techniques (Phillips et al., 2016). Instead,  
112 landform ages have been assessed based on assumed correlations to distal biological and/or  
113 ice-core-inferred paleoclimatic signatures (Balco et al., 2008; Ballantyne and Stone, 2012;  
114 Borchers et al., 2016; Phillips et al., 2016; Stone et al., 1998), or else tentative correlations to  
115 distal and undated lacustrine sediments and tephrostratigraphy (Small and Fabel, 2015).  
116 Consequently, the reference SLHL production-rate values from these sites exhibit deviation  
117 from published production-rate calibration data sets from elsewhere. This has led to the  
118 question of whether problems with scaling models, or the calibration sites themselves, are  
119 responsible for the discrepancy among Scottish calibration data sets and data sets based on  
120 directly dated landforms from father afield (Phillips et al., 2016).

121           The age of the Rannoch Moor moraine belt is bracketed by maximum- and minimum-  
122 limiting  $^{14}\text{C}$  ages, and thus affords minimum- and maximum-limiting bounds, respectively, on  
123 the regional *in situ* production rate of  $^{10}\text{Be}$ . We (1) present a new geological  $^{10}\text{Be}$  calibration  
124 data set for the central Scottish Highlands; (2) discuss the fit to distal calibration data sets, with  
125 implications for available scaling models; (3) evaluate which previously published production-  
126 rate estimates would produce  $^{10}\text{Be}$  surface-exposure ages that are compatible with the  
127 bracketing  $^{14}\text{C}$  chronology; and (4) address previously published  $^{10}\text{Be}$  data sets from Rannoch  
128 Moor in the context of the results presented here.

129 2. Prior Work

130 Four published calibration data sets exist for the Scottish Highlands. These data are from  
131 Coire Mhic Fearchair, Maol Chean Dearg, Corie nan Arr (Ballantyne and Stone, 2012; Borchers  
132 et al., 2016), and from Glen Roy (Small and Fabel, 2015). Data from Coire Mhic Fearchair, Maol  
133 Chean Dearg, and Corie nan Arr are included in the primary global calibration data set of  
134 Borchers et al. (2016).

135 The three studies at Coire Mhic Fearchair (57.2°N, 5.97°W), Maol Chean Dearg (57.49°N,  
136 5.45°W), and Corie nan Arr (57.4°N, 5.6°W) are all based on <sup>10</sup>Be concentrations measured from  
137 erratic boulders resting on the floors of glacial corries, inboard of late-glacial moraine limits, in  
138 the western Scottish Highlands (Ballantyne and Stone, 2012). For production-rate calibration  
139 purposes, erratic boulders in each of these settings were assigned an ‘independent’ age of  
140 11,700 ± 300 yrs. This assigned independent age was not determined by direct dating of the  
141 calibration landforms, but was instead tied to the assumption that rapid changes in mean-  
142 annual air temperatures at the end of the Younger Dryas stadial, recorded in δ<sup>18</sup>O data derived  
143 from Greenland ice cores and paleo-ecological records in Britain, applied to glacier changes in  
144 Scotland (Ballantyne and Stone, 2012).

145 We note that we have reservations about the underlying assumptions used in these  
146 previous calibration studies that (i) Scottish glacier-margin fluctuations should share the same  
147 signature as isotopic fluctuations recorded in Greenlandic ice, or else by paleo-ecological  
148 proxies, and (ii) that undated glacial geomorphologic landforms can be matched to these  
149 isotopic signatures. Recent studies have shown that air-temperatures recorded in Greenlandic  
150 ice-core proxies are dominated by winter conditions (Broecker, 2006; Buizert et al., 2014;

151 Denton et al., 2005), whereas mountain glaciers are dominantly driven by ablation-season (i.e.,  
152 summer) temperatures (e.g., Mackintosh et al., 2017; Zemp et al., 2015; Rupper and Roe, 2008;  
153 Oerlemans, 2005). Observation of a significant mismatch between the magnitudes of glacier  
154 snowlines and ice-core derived temperatures during late-glacial time led to the hypothesis that  
155 North Atlantic stadials, such as the Younger Dryas (12,900–11,600 yrs ago), were characterized  
156 by extreme seasonality (Denton et al., 2005). By this hypothesis, North Atlantic climate during  
157 the Younger Dryas involved mild summers relative to hyper-cold winters on account of winter  
158 sea-ice expansion over the freshened surface of the northern North Atlantic (Denton et al.,  
159 2005; Schenk et al., 2018). In light of this recent progress in understanding ancient water  
160 isotope changes in Greenland snow (and related re-interpretations of paleotemperature  
161 records from Greenland ice cores), we feel that ‘independent’ age assignments tied indirectly to  
162 paleoclimate proxies in these earlier production-rate studies should be reevaluated. As we  
163 demonstrate below, applying previously published Scottish production-rate calibration datasets  
164 (that are tied to the Greenland ice-core chronology) to the Rannoch Moor  $^{10}\text{Be}$  data from this  
165 study results in  $^{10}\text{Be}$  surface-exposure ages that are too young with respect to the limiting  
166 radiocarbon chronology.

167         The fourth  $^{10}\text{Be}$  production-rate calibration data set from Glen Roy, presented by Small  
168 and Fabel (2015), is based on four  $^{10}\text{Be}$  measurements from a 325-m a.s.l. wave-cut bedrock  
169 bench associated with the classic ‘Parallel Roads of Glen Roy’ (56.99°N, 4.68°W). The wave-cut  
170 shoreline was developed at the edge of a proglacial lake that was dammed by the Spean  
171 paleoglacier at the eastern margin of the WHIF during late-glacial time (Sissons, 1978). Small  
172 and Fabel (2015) considered various nominal ages between  $11,562 \pm 422$  and  $12,013 \pm 267$  yrs

173 for when the 325-m bench was exposed to the cosmic-ray flux, with  $12,013 \pm 267$  yrs deemed  
174 the most likely. Thus an 'independent' age of  $12,013 \pm 267$  yrs has been assigned to the data set  
175 available online from the ICE-D production-rate calibration database (Balco, 2018). These age  
176 assignments are based on the assumption that the 325-m shoreline was developed coevally  
177 with the deposition of varved lacustrine sediments preserved in the Loch Laggan East site – in a  
178 different glacier valley approximately 25 km east of Glen Roy – in which a tephra layer is  
179 preserved (MacLeod et al., 2015). Critical to this independent age assignment is the correlation  
180 of that tephra layer with the Vedde Ash ( $12,121 \pm 114$  yrs; Rasmussen et al., 2006). However,  
181 this correlation has not been verified by geochemical analysis of the tephra, for which there  
182 was insufficient material (MacLeod et al., 2015), nor by radiometric dating of the sediments  
183 (Palmer et al., 2010).

184

### 185 3. Rannoch Moor calibration site: Setting and basis for independent age assignment.

186 Rannoch Moor ( $56.63^{\circ}\text{N}$ ,  $4.77^{\circ}\text{W}$ ;  $\sim 310\text{--}330$  m a.s.l.; Fig. 1) is an extensive, peat-covered  
187 moorland surrounded by high-relief glacially-molded peaks of the southern Grampian  
188 Mountains. By most glaciological reconstructions, Rannoch Moor lay near the center of the  
189 West Highland ice field (WHIF) during late-glacial time and was likely one of the last lowland  
190 regions in Scotland to become deglaciated (Figs. 1 and 2; Golledge, 2010; Golledge et al., 2007;  
191 Lowe and Walker, 1976; Sissons, 1976). The landscape of Rannoch Moor is characterized by  
192 ground moraine and till-mantled ice-scoured bedrock, and features a belt of semi-parallel,  
193 discontinuous moraine ridges that were constructed along the margin of the diminished WHIF  
194 just prior to its final deterioration (Fig. 3). We selected Rannoch Moor as a production-rate

195 calibration site for the following reasons. First, moraine ridges of Rannoch Moor feature  
196 numerous large, rounded, embedded, quartz-rich granitoid boulders that are well-suited for  
197 measuring the amount of *in situ* cosmogenic  $^{10}\text{Be}$  production since the time at which the  
198 boulders were first exposed to the cosmic-ray flux. Second, the timing of deglaciation of this  
199 landscape has been determined by  $^{14}\text{C}$  dating of plant macrofossils recovered from the basal  
200 sediment of intermorainal depressions. Third, bracketing  $^{14}\text{C}$  ages provide a chronology for ice-  
201 marginal landforms that delineate the maximum extent of the WHIF, and thus when Rannoch  
202 Moor would have been fully buried by glacial ice. Taken altogether, the boulder-rich landforms  
203 of Rannoch Moor are well bracketed both by maximum- and minimum-limiting  $^{14}\text{C}$  ages, and  
204 therefore meet the criteria for accurate production-rate determination on the basis of  
205 landforms with direct age control (Phillips et al., 2016).

206

207 3.1 Limiting  $^{14}\text{C}$  age control for the construction of the Rannoch Moor moraine belt.

208

209 3.1.1.  *$^{14}\text{C}$  chronology for the full-bodied WHIF – maximum age control on the Rannoch Moor*  
210 *moraine belt*

211 Twenty-seven  $^{14}\text{C}$  dates on marine macrofossils recovered from 10 exposures in basal  
212 tills and terminal moraines of the WHIF afford maximum-limiting age control for expansion of  
213 the WHIF to its full late-glacial extent. As detailed in Bromley et al. (2018), the dated  
214 macrofossils consist of the shells of marine organisms that inhabited the fjords of Scotland's  
215 Atlantic coast following the retreat of the British ice sheet. The shells and seafloor sediments  
216 were subsequently incorporated into the basal sediments of tidal outlet glaciers during the

217 advance of the WHIF and neighboring Mull ice field, and deposited in terminal moraines and till  
218 sheets (Fig. 2; Bromley et al., 2018).  $^{14}\text{C}$  ages of shell remains range from  $11,190 \pm 80$  to  $12,820$   
219  $\pm 90$   $^{14}\text{C}$  yrs ago and convert to a full  $2\sigma$  age range of 12,600 to 15,000 cal yrs BP (i.e., before  
220 the year C.E. 1950) using the Marine13 radiocarbon calibration curve (Reimer et al., 2013). The  
221 choice of an alternative time-dependent marine- $^{14}\text{C}$  curve reconstructed for late-glacial time  
222 from Norway (Bondevik et al., 2006) yields a similar calibrated age range ( $2\sigma$ ) of 12,400 to  
223 14,600 calendar yrs BP for the whole data set (Bromley et al., 2018). Because these  $^{14}\text{C}$  dates  
224 are on marine shells incorporated into WHIF tills, they constitute maximum-limiting ages for (i)  
225 the advance of the ice field to its outer moraines, (ii) the subsequent recession of the WHIF  
226 margin towards the central Scottish Highlands and Rannoch Moor, (iii) construction of the  
227 Rannoch Moor moraine ridges, and (iv) the final stage of deglaciation of WHIF.

228         Two additional  $^{14}\text{C}$  ages on shells recovered from marine sediments at the Balloch  
229 borehole site (Fig. 2), Vale of Leven, and located just inboard of the terminal moraine of the  
230 Lomond piedmont glacier (a southern outlet of the WHIF), afford stratigraphically consistent  
231 minimum-limiting ages of  $11,050 \pm 45$  and  $11,320 \pm 130$   $^{14}\text{C}$  yrs BP for the construction of, and  
232 initial recession from, that late-glacial limit (Bromley et al., 2018). These ages convert to  $2\sigma$   
233 calibrated age ranges of 12,507–12,692 and 12,595–13,087 cal yrs BP, respectively, using the  
234 Marine13 calibration curve. Bromley et al. (2018) compiled these minimum-limiting  $^{14}\text{C}$  ages  
235 from the Balloch borehole and Rannoch Moor, along with previously published minimum ages  
236 [Figs. 1 and 2, Table 1 (this study), and Table S2 of Bromley et al., 2018), to produce a minimum-  
237 limiting population for the culmination of the WHIF. Together with the population of maximum  
238 ages described above (Fig. 2, Table 1; and Table 1 of Bromley et al., 2018), Bromley et al. (2018)

239 then used a probability distribution function of the interval between the two bracketing  $^{14}\text{C}$   
240 populations to calculate the most probable age ( $12,700 \pm 100$  cal yrs BP) for the culmination of  
241 the late-glacial maximum of the WHIF. Further details of this type of statistical treatment are  
242 described in Kelly et al. (2015). For the purposes of this study, the estimate of  $12,700 \pm 100$  cal  
243 yrs BP for the culmination of the WHIF provides a maximum age for construction of the  
244 Rannoch Moor moraines.

245

### 246 3.1.2. *Minimum $^{14}\text{C}$ chronology for construction of the Rannoch Moor moraine belt*

247 Basal  $^{14}\text{C}$  dates from 13 sediment cores extracted from moraine-dammed basins on  
248 Rannoch Moor provide minimum-limiting age control for the Rannoch Moor moraine belt.  
249 Stratigraphically, these bog-filled basins are located both amongst and proximal to the moraine  
250 ridges sampled for  $^{10}\text{Be}$  (Fig. 1). As detailed by Bromley et al. (2014),  $^{14}\text{C}$  ages are on fragments  
251 of predominantly terrestrial plants (Table 1) that colonized Rannoch Moor following  
252 deglaciation and which were subsequently incorporated into basal lake sediments. The  
253 potentially complicating influence of hardwater effects and/or contamination by 'old' carbon is  
254 considered minimal due to (i) the primarily terrestrial nature of the samples and (ii) removal of  
255 any adhering sediment during preparation (see Bromley et al., 2016). Twenty basal  $^{14}\text{C}$  ages  
256 from the 13 cores range from  $9140 \pm 180$  to  $10,550 \pm 65$   $^{14}\text{C}$  yrs BP, corresponding to a  $2\sigma$   
257 calibrated (IntCal13; Reimer et al., 2013) range of 9701–12,648 cal yrs BP for the full data set  
258 (Table 1; Bromley et al., 2014). Here, adhering to the principles of stratigraphy (e.g., Strelin et  
259 al., 2011), we use the oldest, and thus closest, minimum-limiting  $^{14}\text{C}$  age for deglaciation of  
260 Rannoch Moor (sample OS-99685 from core RM-12-3A;  $12,480 \pm 100$  cal yrs BP weighted mean

261 calibrated age) for determining the local production rate. Reinforcing this  $^{14}\text{C}$  measurement,  
262 and thus its suitability for bracketing the Rannoch Moor moraine, we note that this single age  
263 determination aligns closely with the next-youngest ages in the data set reported by Bromley et  
264 al. (2014). Specifically, four statistically indistinguishable  $^{14}\text{C}$  ages from core RM-10-3A provide  
265 an earliest probable age of 12,490 cal yrs BP for plant growth (and thus deglaciation) based on  
266 the 90% confidence interval of their summed probability (see Bromley et al., 2014). The high  
267 degree of internal consistency among these five oldest  $^{14}\text{C}$  ages, therefore, supports our model  
268 that Rannoch Moor was ice free by  $12,480 \pm 100$  cal yrs BP. All  $^{14}\text{C}$  sample details are given in  
269 Table 1.

270

### 271 3.1.3. Midpoint age for construction of Rannoch Moor moraines

272 Based on the statistical assessment of maximum- and minimum-limiting  $^{14}\text{C}$  ages  
273 presented by Bromley et al. (2018), we take their most probable age of  $12,700 \pm 100$  cal yrs BP  
274 (see Section 3.1.1, above) for the culmination of the full late-glacial WHIF (Bromley et al., 2018)  
275 as a maximum-limiting age for the construction of the Rannoch Moor moraine belt. We then  
276 take the single oldest age of the Rannoch Moor  $^{14}\text{C}$  data set (Bromley et al., 2014) to provide  
277 the closest minimum-limiting age of  $12,480 \pm 100$  cal yrs BP for the construction of the Rannoch  
278 Moor moraine belt. From the bracketing  $^{14}\text{C}$  ages, we take a midpoint value of  $12,590 \pm 140$  cal  
279 yrs BP to represent a likely age of exposure of the Rannoch Moor moraine belt (Fig. 4). The  
280 uncertainty of this midpoint rate is determined by propagating in quadrature the uncertainties  
281 for the respective maximum and minimum age bounds. We note that this uncertainty is slightly  
282 greater than the range of the maximum- and minimum-limiting ages. Taken together with  $^{10}\text{Be}$

283 concentrations measured in the surfaces of embedded glacial boulders, these limits and  
284 corresponding midpoint for the age of the Rannoch Moor moraine belt provide the basis for  
285 production-rate calibration, described below.

286

## 287 4. Methods

288 Our field and laboratory procedures for obtaining in situ  $^{10}\text{Be}$  concentrations for  
289 production-rate determination followed those reported in Schaefer et al. (2009), Putnam et al.  
290 (2010b) and Kaplan et al. (2011), and are described online at  
291 <http://www.ldeo.columbia.edu/tcn>. Methods for developing the  $^{14}\text{C}$  chronology of the WHIF  
292 and Rannoch Moor deglaciation are reported in Bromley et al. (2018; 2014).

293

### 294 4.1 Field Methods

295 Samples were collected for  $^{10}\text{Be}$  analysis in April of C.E. 2010. We targeted for sampling  
296 the surfaces of boulders rooted in discontinuous ridge segments of the Rannoch Moor moraine  
297 belt (Fig. 3). Nine  $^{10}\text{Be}$  samples (RM-10-01 to 09) are from the outermost moraine ridge of this  
298 belt, which is immediately outboard of core sites RM-10-1A, RM-10-1C, RM-10-1D, RM-12-4A,  
299 RM-12-4B, RM-12-5, and RM-10-3A (Fig. 1; Bromley et al., 2014). Core sites RM-12-2A, RM-12-  
300 2B, RM-13-3 and K3 [sampled by Walker and Lowe (1977)] are from a kettle-hole bog within a  
301 discontinuous moraine ridge segment also associated with this outboard ridge. Boulders  
302 associated with the outermost moraine ridge of the Rannoch Moor belt would have begun their  
303 exposure to the cosmic-ray flux prior to the accumulation of plant macrofossils that we  
304 targeted for  $^{14}\text{C}$  dating.

305 We also collected four samples for  $^{10}\text{Be}$  analysis (RM-10-10 to -13) from a subparallel set  
306 of discontinuous moraine ridges located just inside of the outermost ridges; three of these  
307 samples were selected for  $^{10}\text{Be}$  analysis (RM-10-10, RM-10-11, and RM-10-12). These  $^{10}\text{Be}$   
308 sampling locations are immediately inboard of the aforementioned coring locations, with the  
309 closest core sites being RM-10-1A, RM-10-1C, RM-10-1D, RM-12-4A, RM-12-4B, RM-12-5, and  
310 RM-10-3A. All  $^{10}\text{Be}$  sample locations are outboard of core sites RM-12-1, RM-12-2A, RM-13-2B,  
311 and RM-13-3, as well as the earliest core sites K1 and K2 that were previously reported by  
312 Walker and Lowe (1977, 1979).

313 We sampled boulders that are well-embedded in geomorphologically stable positions at  
314 the crests of moraine ridges (Fig. 5). We avoided boulders located in sites that may have been  
315 disturbed by non-glacial post-depositional surface processes. Sampled surfaces were typically  
316 from the tops of well-rounded granitoid boulders. Deeply pitted, exfoliating, and/or spalled  
317 surfaces were avoided. We targeted surfaces that retained patches of glacial polish, glacially  
318 polished mineral grains, and/or glacial striae, all of which indicate minimal surface weathering  
319 since the time of deposition. Samples were collected using the drill-and-blast technique (Kelly,  
320 2003) along with hammer and chisel. For each boulder sampled, we measured clast dimensions  
321 (long axis, short axis, and sample location height above ground measured on four sides), strike  
322 and dip, topographic shielding (measured azimuth and elevation at every inflection point on the  
323 skyline), and GPS coordinates. All sampled boulders were described, drawn, and photographed  
324 from every side.

325 We determined sample elevations from the Shuttle Radar Topography Mission (SRTM)  
326 digital elevation model in Google Earth in combination with the local Ordnance Survey 1:25,000

327 scale topographic map sheet with a contour interval of 10 m (Ordnance Survey, 2015). We  
328 found that Google Earth-derived elevations align well with contours plotted in the topographic  
329 map. All reported elevations are therefore derived from Google Earth and should be considered  
330 accurate to within  $\pm 5$  m (based on topographic map contours).

331

## 332 4.2 Laboratory Methods

333         Following field collection, samples were shipped to the Lamont-Doherty Earth  
334 Observatory (LDEO) Cosmogenic Nuclide Laboratory for mineral separation and beryllium  
335 extraction using standard protocols. Mass-weighted sample thicknesses were measured using  
336 digital calipers. Samples were subsequently crushed, pulverized, and sieved to a grain-size  
337 range of 125–710  $\mu\text{m}$ . These sample fractions were then subjected to boiling in concentrated  
338  $\text{H}_3\text{PO}_4$  and NaOH solutions. Some samples were further treated with froth-floatation mineral-  
339 separation techniques to separate feldspar. All samples were treated to successive etches in 2%  
340 HF/2%  $\text{HNO}_3$  and 5% HF/5%  $\text{HNO}_3$  solutions until only pure quartz remained. Pure quartz  
341 fractions were then weighed, spiked with  $\sim 180$   $\mu\text{g}$  of LDEO low- $^{10}\text{Be}$ -background Be carrier, and  
342 then dissolved in concentrated (49%) HF. We used LDEO carrier 5 (initial  $^9\text{Be}$  concentration =  
343  $1024 \pm 10$  ppm, based on multiple measurement). To correct for the increase in concentration  
344 of the carrier over time due to evaporation, the weight of the carrier bottle was recorded  
345 before and after each use. We calculated the percent change in weight and multiplied by the  
346 last corrected carrier concentration. This percent of concentration is added to the previous  
347 concentration to arrive at the corrected concentration. The weight loss between uses of the  
348 carrier solution is typically only a few milligrams, amounting to only a few 100ths of a percent,

349 but this amounts to an increase in concentration of approximately 2% over 5 years. The rate of  
350 evaporation increases as the volume of solution remaining in the bottle decreases, and  
351 therefore the increase in concentration with time is not linear. The LDEO carrier  $^9\text{Be}$   
352 concentration was corrected for evaporation each time carrier was added to samples (see  
353 Tables 2 and 3 for corrected carrier concentrations).

354 After dissolution, beryllium was then separated from other common ions using ion-  
355 chromatography techniques based on Kohl and Nishiizumi (1992) and following the procedures  
356 from the University of Washington and Lamont-Doherty Earth Observatory laboratories,  
357 available online at: <http://depts.washington.edu/cosmolab/chem.shtml> and  
358 <http://www.ldeo.columbia.edu/tcn>. Each resulting BeO sample was combined with Nb powder,  
359 packed into stainless steel targets, and submitted to the Lawrence-Livermore National  
360 Laboratory Center for Accelerator Mass Spectrometry (LLNL CAMS) for  $^{10}\text{Be}/^9\text{Be}$  measurement.  
361 Sample  $^{10}\text{Be}/^9\text{Be}$  ratios were measured relative to the 07KNSTD3110 standard ( $^{10}\text{Be}/^9\text{Be} = 2.85$   
362  $\times 10^{-12}$ ; Nishiizumi et al., 2007), and corrected for boron contamination and machine  
363 backgrounds (each correction was typically <1%).

364 We determined  $^{10}\text{Be}$  concentrations for 12 samples from the Rannoch Moor moraines.  
365 Samples were processed in six laboratory batches and measured in six CAMS runs spread over  
366 the course of five years (C.E. 2012–2016). To evaluate  $^{10}\text{Be}$  contamination during laboratory  
367 procedures, we measured nine procedural laboratory blanks. The blanks afford  $^{10}\text{Be}$  values that  
368 range between 570 and 11,970  $^{10}\text{Be}$  atoms per blank and yield an arithmetic mean of  $4570 \pm$   
369  $3460$  atoms ( $\pm 1\sigma$ ). Blank concentrations correspond to <1% of the total number of  $^{10}\text{Be}$  atoms  
370 measured in our samples in the range of 1,000,000 atoms  $^{10}\text{Be}$ . Reported  $^{10}\text{Be}$  concentration

371 uncertainties (Table 2) include the reported analytical uncertainty ( $1\sigma$ ) propagated with  
372 uncertainties related to machine background, procedural blank, and boron corrections.  
373 Uncertainties related to background, blank, and boron corrections are each  $<1\%$ . Reported  $^{10}\text{Be}$   
374 concentration uncertainties are  $\sim 2\%$  ( $1\sigma$ ). Uncertainties related to  $^9\text{Be}$  carrier concentration  
375 ( $\sim 1\%$ ) were treated as systematic errors and incorporated into uncertainties calculated for the  
376 data set as a whole (and also propagated with production-rate uncertainties).

377

#### 378 *4.3 Production-rate calculation*

379 Maximum- and minimum-limiting production rate values were calculated by comparing  
380  $^{10}\text{Be}$  concentrations measured in morainal boulders at Rannoch Moor with minimum- and  
381 maximum-limiting calendar-year-converted  $^{14}\text{C}$  age constraints, respectively. The midpoint  
382 production-rate value was determined by comparing  $^{10}\text{Be}$  concentrations with the age  
383 corresponding to the midpoint of the bracketing limiting ages (and uncertainty corresponding  
384 to the range of bracketing ages). Topographic shielding correction factors were calculated using  
385 the University of Washington (UW) online calculators available at:  
386 <https://hess.ess.washington.edu>.

387 We assume that erosion has been negligible (at least for the sampled surfaces) since the  
388 boulders were deposited, based on field observations of glacially polished surfaces/mineral  
389 grains present on sampled boulders. Likewise, winter snow cover is generally ephemeral at the  
390 elevations of the boulders sampled, and the open landscape of Rannoch Moor is susceptible to  
391 strong winds that would keep the boulders largely free of snow. We also note that any effects  
392 of erosion or snow cover would not necessarily be consistent from sample to sample and would

393 likely increase the scatter among the  $^{10}\text{Be}$  concentrations. Thus, we take the tight agreement  
394 among the  $^{10}\text{Be}$  concentrations determined from the Rannoch Moor boulders (reported below)  
395 to indicate negligible impacts of erosion or snow cover on this dataset. Therefore, consistent  
396 with previous production-rate calibration efforts (e.g., Balco et al., 2009; Kaplan et al., 2011;  
397 Kelly et al., 2015; Putnam et al., 2010b; Young et al., 2013), the production-rate and exposure-  
398 age calculations reported below do not include corrections for erosion or snow cover.

399         Following previous studies (Balco et al., 2009; Kaplan et al., 2011; Putnam et al., 2010b;  
400 Young et al., 2013), we do not apply any correction for uplift in our production-rate or  
401 exposure-age calculations. Although there has been a viscoelastic response of the Earth's  
402 lithosphere to deglaciation in this region, the signature of post-glacial isostatic adjustment in  
403 central Scotland has been relatively minor compared to other production-rate calibration sites  
404 targeting deglaciated landscapes (e.g., Balco et al., 2009; Young et al., 2013). For example, the  
405 central Scottish Highlands have experienced only ~10 m or so of total vertical displacement  
406 with respect to modern sea level over the period of exposure and have been uplifting ~1 mm yr<sup>-1</sup>  
407 over the past 1000 yrs or so (Lambeck, 1991; Stockamp et al., 2016)]. In addition, it is unclear  
408 how changes in air pressure related to deglaciation and eustatic sea-level rise may have  
409 counteracted the effects of uplift on production rates (Young et al., 2013). For these reasons we  
410 chose not to subject production-rate calculations to an uplift correction.

411         All production-rate determinations were calculated using Version 3 of the online UW  
412 cosmogenic calculators (<https://hess.ess.washington.edu>). This version of the calculator is  
413 broadly similar to earlier versions employed in previous production-rate calibration studies  
414 (e.g., Balco et al., 2009; Balco et al., 2008; Kaplan et al., 2011; Kelly et al., 2015; Putnam et al.,

415 2010b; Young et al., 2013), but includes a few updates. Arguably the most important update to  
416 Version 3 of the UW calculator is the implementation of a revised (and simplified) calculation  
417 for muon production (Balco, 2017; Braucher et al., 2013). This muon production model replaces  
418 the Heisinger et al. (2002a; 2002b) protocols used in previous versions of the calculator, which  
419 were based on laboratory irradiation experiments. The Balco et al. (2017) model predicts a SLHL  
420 muon production rate of  $0.0735 \text{ at g}^{-1} \text{ yr}^{-1}$ , which, for example, accounts for only 1.8% of total  
421 production if the SLHL neutron spallation rate at a rock surface is  $4.0 \text{ at g}^{-1} \text{ yr}^{-1}$  (and 1.9% if the  
422 reference SLHL neutron spallation rate is  $3.9 \text{ at g}^{-1} \text{ yr}^{-1}$ ). To determine the SLHL 'reference'  
423 production rate for neutron spallation only, the UW production-rate calculator first subtracts  
424 the muonogenic component, scaled for latitude and altitude, from the total measured  $^{10}\text{Be}$   
425 production. The remaining (~98%) of the  $^{10}\text{Be}$  is referenced to SLHL, or else evaluated against a  
426 modeled local reference production-rate value, using one of three scaling models (described  
427 below) to determine the neutron-produced component of the total  $^{10}\text{Be}$  inventory.

428         It is important to note that the Balco (2017) protocol for determining  $^{10}\text{Be}$  production by  
429 muons predicts a lower muon production rate than the previously implemented Heisinger et al.  
430 (2002a; 2002b) framework. As such, all reported values for neutron spallation production rates  
431 calculated with Version 3 of the UW online production-rate calculator are systematically ~2%  
432 higher than previously reported values. However, because muon production accounts for such  
433 a small percentage of surface production, this procedural change has virtually no impact on  
434 surface-exposure chronologies calculated using the same production-rate calibration data sets  
435 but with previous versions of the UW calculator (although studies of erosion rates or burial may  
436 be affected).

437 Version 3 of the UW calculator references an atmosphere model based on the ERA-40  
438 Reanalysis data set (Uppala et al., 2005) for site-specific air-pressure information, and includes  
439 the Lifton et al. (2014) scaling model ('LSDn') in addition to the Lal (1991)/ Stone (2000) ('St')  
440 and Lal / Stone time-dependent ('Lm') models used in previous versions of the calculator. Full  
441 documentation of Version 3 of the UW calculators is available online at:  
442 <https://sites.google.com/a/bgc.org/v3docs/>.

443 In order to facilitate comparison of production-rate calibration sites at different  
444 locations, we used Version 3 of the UW online calculator to determine production rates  
445 referenced to SLHL using the 'St' and 'Lm' scaling models. Because the LSDn model produces  
446 site-specific production rates (in atoms  $\text{g}^{-1} \text{yr}^{-1}$ ) as opposed to non-dimensional scaling factors  
447 that apply to reference SLHL production rates (such as with the St and Lm scaling models), and  
448 because the reference production rates used in the LSDn model differ from those of the other  
449 models (related to how the LSDn model accounts for solar variability), the UW online calculator  
450 provides a non-dimensional correction factor that represents the offset between the  
451 independently calibration production rate and that determined by the LSDn model (G. Balco,  
452 personal communication, 10 September 2017). Therefore, to maintain consistency with the  
453 reporting procedures of the UW online calculators, we also report non-dimensional correction  
454 factors for the LSDn production-rate scaling model rather than SLHL reference production-rate  
455 values, as output by Version 3 of the UW online calculator.

456 Production-rate uncertainties attending the Rannoch Moor results are calculated by the  
457 'total scatter' method in Version 3 of the UW online calculator. This method accounts for the  
458 standard deviation of the individual measurements, as well as the  $\chi^2$  of the population with

459 respect to a best-estimate value. We also incorporate a 1% carrier-concentration uncertainty  
460 into the overall Rannoch Moor production-rate uncertainty estimate (i.e., propagated in  
461 quadrature with the total-scatter uncertainty).

462 To maintain consistency with the production-rate calculations employed for the  
463 Rannoch Moor data set, we re-calculated production rates and attendant uncertainties from  
464 previously published calibration data sets using these same methods. SLHL production rates  
465 and correction factors for previously published calibration data sets have also been calculated  
466 using Version 3 of the UW online calculator with the data tables supplied by the ICE-D  
467 production-rate calibration database (<http://calibration.ice-d.org>). For single-site calibration  
468 sites, we employed the ‘total scatter’ method for determining uncertainties. For production-  
469 rate calculations involving previously published calibration data sets based on multiple sites,  
470 uncertainties were determined using the ‘site-to-site scatter’ calculation in the online  
471 calculator, which is derived from the standard deviations of each calibration site and the  
472 corresponding  $\chi^2$  for the best-estimate value of the combined data sets (see the  
473 documentation for Version 3 of the UW online calculators for a complete explanation of  
474 uncertainty determinations: [https://sites.google.com/a/bgc.org/v3docs/home/2-input-and-](https://sites.google.com/a/bgc.org/v3docs/home/2-input-and-output)  
475 [output](https://sites.google.com/a/bgc.org/v3docs/home/2-input-and-output)).

476 We note that the site-to-site averaging method employed in the UW online production-  
477 rate calculator differs slightly from the method employed in Borchers et al. (2016). Whereas the  
478 calculation of Borchers et al. (2016) weights sites by the precision of independently known  
479 landform ages, the averaging method employed in Version 3 of the UW online production-rate  
480 calculator weights all sites equally (Balco, personal communication, 25 June 2018). Thus, the

481 calibration results reported here for the Borchers et al. (2016) data set may differ slightly from  
482 those reported in the original paper. In addition, we note that we removed a small number of  
483 apparent outlier measurements (determined from Version 3 of the UW online calculator, based  
484 on  $\chi^2$  statistics) from three data sets before calculating production rates: One anomalously low-  
485 concentration measurement from the data set of Kaplan et al. (2011; sample EQ-08-04), two  
486 anomalously high-concentration samples from the dataset of Martin et al. (2015; samples AZA-  
487 30 and AZA-32), and one anomalously high-concentration sample and one anomalously low-  
488 concentration sample from the data set of Claude et al. (2014; samples CHI-11 and CHI-10).  
489 Finally, to maintain consistency with the approach outlined above, we did not include any  
490 corrections for erosion, snow cover, or uplift in our analysis of these previously published data  
491 sets.

492

## 493 5. Results

### 494 5.1 $^{10}\text{Be}$ data

495 Measured  $^{10}\text{Be}$  concentrations exhibit tight internal consistency and form an  
496 approximately normal distribution when corrected for thickness and topographic shielding.  
497 Uncorrected concentrations range from  $6.66 \pm 0.22$  to  $7.70 \pm 0.15$  [ $\times 10^4$ ] at  $\text{g}^{-1} \text{yr}^{-1}$  (Table 2).  
498 Only one measurement (RM-10-01;  $7.70 \pm 0.15$  [ $\times 10^4$ ]) has a distinguishably different (i.e.,  
499 higher) concentration from the rest of the population. If treated as a surface-exposure age (as a  
500 means of normalizing the measurements for the effects of pressure elevation, sample  
501 thickness, topographic shielding, etc.), the corresponding age is distinguishably older than the  
502 rest of the data set and is flagged as an outlier by Version 3 of the UW online exposure age

503 calculator (Balco et al., 2008; and subsequent updates). Therefore, we consider this  
504 measurement to be an outlier and exclude it from further assessment of production rates or  
505 exposure ages. The remaining eleven samples yield uncorrected concentrations ranging from  
506  $6.66 \pm 0.22$  to  $7.35 \pm 0.18$  [ $\times 10^4$ ] at  $\text{g}^{-1}$ , with an arithmetic mean of  $7.01 \pm 0.23$  [ $\times 10^4$ ] atoms  $\text{g}^{-1}$   
507 ( $N = 11$ ; uncorrected for thickness or topographic shielding; uncertainty is  $1\sigma$  propagated in  
508 quadrature with a conservative 1% systematic uncertainty related to carrier concentration). The  
509 arithmetic mean of the thickness- and shielding-corrected concentrations is  $6.93 \pm 0.24$  [ $\times 10^4$ ]  
510 at  $\text{g}^{-1}$  and yields a reduced- $\chi^2$  value of 1.89. Although this latter arithmetic mean value accounts  
511 for sample thickness and topographic shielding, the constituent concentrations are not  
512 corrected for minor differences in sample elevation from 313 to 327 m a.s.l. The striking  
513 internal consistency (and low- $\chi^2$  value) indicate that the remaining scatter in the  $^{10}\text{Be}$   
514 concentrations of the individual samples can be explained by analytical uncertainties (Balco and  
515 Schaefer, 2006; Bevington and Robinson, 1992).

516

## 517 5.2 $^{10}\text{Be}$ production rates

518 Dividing the arithmetic mean of the measured  $^{10}\text{Be}$  concentrations of  $6.92 \pm 0.24$  [ $\times 10^4$ ]  
519 atoms  $\text{g}^{-1} \text{yr}^{-1}$  by the midpoint age of  $12,590 \pm 140$  yrs for the Rannoch Moor moraine belt yields  
520 the total local  $^{10}\text{Be}$  production rate of  $5.50 \pm 0.18$  at  $\text{g}^{-1} \text{yr}^{-1}$  (this value is not yet corrected for  
521 elevation differences among sampled surfaces). This result was then transformed to SLHL  
522 values using the scaling models incorporated into Version 3 of the UW online production-rate  
523 calculator and removed of the muon-produced  $^{10}\text{Be}$  component. All SLHL production-rate  
524 results reported here are therefore for neutron spallation only and summarized in Table 4. The

525 non-time-dependent 'St' scaling model yields SLHL reference maximum, minimum, and  
526 midpoint  $^{10}\text{Be}$  production rates of  $<3.95 \pm 0.11$  at  $\text{g}^{-1} \text{yr}^{-1}$ ,  $>3.88 \pm 0.11$  at  $\text{g}^{-1} \text{yr}^{-1}$ , and  $3.91 \pm 0.11$   
527 at  $\text{g}^{-1} \text{yr}^{-1}$ , respectively. The time-dependent 'Lm' scaling model yields SLHL reference maximum,  
528 minimum, and midpoint  $^{10}\text{Be}$  production rates of  $<3.95 \pm 0.11$  at  $\text{g}^{-1} \text{yr}^{-1}$ ,  $>3.89 \pm 0.11$  at  $\text{g}^{-1} \text{yr}^{-1}$ ,  
529 and  $3.92 \pm 0.11$  at  $\text{g}^{-1} \text{yr}^{-1}$ , respectively. Finally, the time-dependent 'LSDn' scaling model yields  
530 maximum, minimum, and midpoint  $^{10}\text{Be}$  production-rate correction factors of  $<0.787 \pm 0.023$  at  
531  $\text{g}^{-1} \text{yr}^{-1}$ ,  $>0.773 \pm 0.022$  at  $\text{g}^{-1} \text{yr}^{-1}$ , and  $0.780 \pm 0.022$  at  $\text{g}^{-1} \text{yr}^{-1}$ , respectively. All production-rate  
532 calculations yield low  $\chi^2$  values between 11.07 and 11.42 relative to an expected theoretical  
533 value for a Gaussian distribution of the same population size.

534 Input data sets for use with the UW online exposure calculators are provided as online  
535 Supplementary Material to this paper.

536

## 537 6. Discussion

538 Here we discuss the calibration data set presented in this study within the context of: (i) distal  
539 calibration data sets based on landforms with direct independent age control, (ii) previously  
540 published calibration data sets from indirectly dated landforms in the Scottish Highlands, and  
541 (iii) previously published  $^{10}\text{Be}$  data sets from the Rannoch Moor region.

542

### 543 6.1. Comparison to distal $^{10}\text{Be}$ production-rate calibration data sets

544 Here, we evaluate how the Rannoch Moor calibration data set aligns with other  
545 comparable calibration efforts from around the world. Tables 5 and 6 compare SLHL production  
546 rates (for 'St' and 'Lm' scaling models) and production-rate correction factors (for 'LSDn')

547 scaling) reported in this study for Rannoch Moor with previously published production-rate  
548 calibration sites from different latitudes and altitudes with absolute independent age  
549 constraints. Figure 6 compares the results of all calibration data sets for the three scaling  
550 models and normalized to Rannoch Moor values. All SLHL production-rate values (and LSDn  
551 correction factors) have been calculated using Version 3 of the UW online production-rate  
552 calculator. Specifically, we compare the Rannoch Moor data set with those from northeastern  
553 North America (Balco et al., 2009), the Canadian Arctic (i.e., Baffin Bay; Young et al., 2013),  
554 Switzerland (Claude et al., 2014), Peru (Kelly et al., 2015; Martin et al., 2015), New Zealand  
555 (Putnam et al., 2010b), and southern South America (Kaplan et al., 2011). In addition, for  
556 reference, we consider production rates from the primary global calibration data set of  
557 Borchers et al. (2016; also the default calibration data set in Version 3 of the UW online  
558 calculator) which includes some  $^{10}\text{Be}$  measurements from landforms that are not directly dated  
559 (see section 2.0, above).

560         In general, when scaled using currently accepted protocols, the results reported here for  
561 the Rannoch Moor  $^{10}\text{Be}$  calibration site agree well with results from calibration sites with  
562 comparable independent age control, mentioned above (Tables 5 and 6; Fig. 6). All scaling  
563 models produce reasonably good agreement. The best overall empirical agreement among  
564 these disparate sites is achieved with the non-time-dependent ‘St’ scaling protocol. By this  
565 scaling method, all of the regional calibrations yield production-rate values that agree with the  
566 Rannoch Moor value, within respective uncertainties. The best empirical agreement is between  
567 the Rannoch Moor and New Zealand values. The time-dependent ‘Lm’ scaling model yields  
568 general agreement among Rannoch Moor and other middle and high-latitude sites, but with

569 less coherence among the Rannoch Moor and tropical/high-altitude (Peruvian) data sets. The  
570 'LSDn' scaling model produces the least amount of convergence among production-rate  
571 correction factors determined from Rannoch Moor and other comparable calibration data sets.  
572 Whereas results from sites in the Southern Hemisphere, tropics, and Switzerland tend to show  
573 close agreement among one another, those sites exhibit little to no overlap with the result from  
574 Rannoch Moor (considering respective uncertainties). On the other hand, the result from Baffin  
575 Bay shows close agreement with that from Rannoch Moor when calculated using the LSDn  
576 scaling model.

577         The Rannoch Moor calibration data set presented here yields SLHL production-rate  
578 values for 'St' and 'Lm' scaling models, and a production-rate correction factor for the 'LSDn'  
579 model, that are 5%, 7%, and 8% lower, respectively, than the globally averaged values  
580 determined from the primary calibration data set of Borchers et al. (2016). Using our <sup>10</sup>Be data  
581 from Rannoch Moor, the primary calibration data set of Borchers et al. (2016) produces  
582 surface-exposure ages that are 2-5% too young with respect to minimum-limiting <sup>14</sup>C-age  
583 constraints (depending on the scaling model used).

584         We note that the production-rate calibration data set presented here eliminates the  
585 unexplained discordance among production-rate calibrations from Scotland and elsewhere on  
586 Earth, as identified by Phillips et al. (2016). Whereas this discrepancy was previously attributed  
587 to problems relating to scaling models, perhaps involving anomalous changes in atmospheric  
588 pressure related to deglaciation, we hypothesize that the scaling models do a reasonably good  
589 job of reconciling calibration data that are based solely on landforms with direct radiometric  
590 chronological control.

591

592 *6.2. Comparison with other Scottish calibration data sets*

593           Table 6 provides SLHL production rates and correction factors determined from the  
594 Coire Mhic Fearchair, Maol Chean Dearg, Corie nan Arr, and Glen Roy data sets, for comparison  
595 to the results presented in this study from Rannoch Moor. Overall, these previously published  
596 calibration data sets yield SLHL production-rate estimates/correction factors that are ~6–8%  
597 higher (depending on choice of scaling model, with erosion rates set to zero) than our Rannoch  
598 Moor calibration data set, based on the midpoint age assignment, and ~4–7% higher than the  
599 maximum-limiting production rate determined from Rannoch Moor (based on minimum-  
600 limiting <sup>14</sup>C data for plant colonization). See Table 6b for comparison of production-rate ratios.  
601 Inclusion of erosion rates proposed in the original publications further increases the offsets by  
602 ~1%. The discrepancy in production-rate estimates translates to surface-exposure ages that are  
603 at least 4–7% too young to be consistent with the independent <sup>14</sup>C chronology at Rannoch  
604 Moor. We consider that this observed disagreement between <sup>14</sup>C and <sup>10</sup>Be chronologies can be  
605 explained by calibration landforms having older ages than initially assumed in previous  
606 calibration studies (Ballantyne and Stone, 2012; Borchers et al., 2016).

607           An additional observation is that the Coire Mhic Fearchair, Maol Chean Dearg, and Corie  
608 nan Arr data sets (Ballantyne and Stone, 2012; Borchers et al., 2016) yield surface-exposure  
609 chronologies that are indistinguishable from that at Rannoch Moor when all ages are calculated  
610 using a common production-rate calibration data set. For example, when using the Rannoch  
611 Moor production-rate calibration data set (this study) and ‘St’ scaling, we obtain arithmetic  
612 mean ages [ $\pm 1\sigma$ ] of  $12,710 \pm 650$  yrs,  $12,510 \pm 150$  yrs, and  $12,620 \pm 330$  yrs for the Coire Mhic

613 Fearchair, Maol Chean Dearg, Corie nan Arr data sets, respectively. Compared to the mean  $^{10}\text{Be}$   
614 surface-exposure value obtained for Rannoch Moor of  $12,650 \pm 340$  yrs (using the same  
615 calculation method), all data sets are statistically indistinguishable within respective  
616 uncertainties, with arithmetic mean values deviating by only 200 yrs or less. Choice of a  
617 different scaling model does not alter this result. Therefore, the hypothetical case can be made  
618 that the erratic boulders sampled from the corrie glacier systems described in Ballantyne and  
619 Stone (2012) were all exposed, and hence deglaciated, at the same time as Rannoch Moor,  
620 within respective uncertainties.

621         When recalculating the Glen Roy  $^{10}\text{Be}$  chronology (Small and Fabel, 2015) using the  
622 Rannoch Moor production-rate calibration data set presented here, surface-exposure ages  
623 from the ~325-m shoreline at Glen Roy (one sample with a 50-cm peat cover was omitted,  
624 consistent with treatment of this data set in the ICE-D database) afford an arithmetic mean  
625 value of  $13,060 \pm 130$  yrs [ $\pm 1\sigma$ ]. This landform age is consistent with the range of  $^{14}\text{C}$  ages  
626 obtained for the WHIF moraines and tills reported in Bromley et al. (2018).

627

### 628 *6.3 Comparison with other $^{10}\text{Be}$ data from Rannoch Moor*

629         Two previous studies provided  $^{10}\text{Be}$  data from the Rannoch Moor region and afford an  
630 opportunity for interlaboratory and inter-AMS comparison with [ $^{10}\text{Be}$ ] data presented in this  
631 study. The first  $^{10}\text{Be}$  data from this area, published by Golledge et al. (2007), were from erratic  
632 boulders mantling the nearby summit ridge of Beinn Inverveigh (~580 – 620 m a.s.l.), located  
633 approximately 10 km SSW of Rannoch Moor. Beinn Inverveigh has been variably mapped as  
634 having stood above the full-bodied late-glacial WHIF (Thorp, 1984; Thorp, 1986), or as having

635 been fully ice-covered by the WHIF (Golledge, 2007). The chronology of erratic boulders was  
636 therefore used to determine the thickness of the WHIF at its full late-glacial configuration  
637 (Golledge, 2007, 2010; Golledge et al., 2007). In any case, these higher-elevation boulders  
638 would have been exposed to the cosmic-ray flux prior to the boulders rooted in the Rannoch  
639 Moor moraine belt, which were exposed during the final phase of WHIF disintegration. Thus,  
640 this morphostratigraphic age difference should be reflected in the measured [ $^{10}\text{Be}$ ] inventory of  
641 these data sets. Calculation of the Golledge et al. (2007)  $^{10}\text{Be}$  surface-exposure data set using  
642 the Rannoch Moor calibration data set yields ages of  $13,270 \pm 880$  yrs (BI 1),  $14,280 \pm 620$  yrs  
643 (BI 2),  $14,760 \pm 800$  yrs (BI 3), and  $14,600 \pm 1400$  yrs (BI 4) documenting the height of the WHIF  
644 during late-glacial time (ages were corrected for AMS standardization and calculated using St  
645 scaling in Version 3 of the UW online calculator, for illustrative purposes, although all scaling  
646 models afford similar ages, given the proximity of the samples to the Rannoch Moor calibration  
647 site). These results are morphostratigraphically concordant with the  $^{10}\text{Be}$  data presented here,  
648 and are also in agreement with the span of  $^{14}\text{C}$  ages on WHIF tills and moraines marking  
649 advances toward full late-glacial limits between  $\sim 14,600$  and  $12,800$  cal. yrs ago (Bromley et al.,  
650 2018). Thus, the data set of Golledge et al. (2007) may serve to constrain the height of the full-  
651 bodied WHIF of late-glacial time.

652 In addition, Small and Fabel (2016b) presented a  $^{10}\text{Be}$  dataset from boulders rooted in  
653 the same Rannoch Moor moraine belt targeted here, and in one case from the same boulder  
654 sampled by our team in C.E. 2010. Overall, the Small and Fabel (2016b) data set exhibits good  
655 internal consistency, with a tight cluster of four surface-exposure ages and two older samples  
656 rejected as outliers. On the basis of this data set, Small and Fabel (2016b) suggested that,

657 regardless of which production-rate calibration data set is used, none is sufficient to produce a  
658  $^{10}\text{Be}$  chronology for their data set that is compatible with the minimum-limiting  $^{14}\text{C}$  dates at  
659 Rannoch Moor. This apparent discordance led the authors to question the validity of the  
660 Rannoch Moor  $^{14}\text{C}$  data set, which in turn triggered a comment and reply that discussed some  
661 of the underlying issues in greater detail (Bromley et al., 2016; Small and Fabel, 2016a).

662 We report the observation that the [ $^{10}\text{Be}$ ] concentrations presented here are  
663 systematically higher than those reported by Small and Fabel (2016b). Comparison of the mean  
664 values of the [ $^{10}\text{Be}$ ] distributions (pruned of outliers and corrected for thickness and shielding)  
665 yields an offset of 7.7%. The difference increases slightly to 7.9% when accounting for  
666 differences in sample elevation (this was achieved by calculating nominal exposure ages for the  
667 whole data set using the St scaling protocol and the Rannoch Moor production rate presented  
668 here; Fig. 7). A  $\chi^2$  test of the combined data sets (minus outliers) yields an overall  $\chi^2$  value of  
669 49.96. When compared to the theoretical expected value of 23.68 for a Gaussian distribution of  
670 the same population size (evaluated at 95% confidence), this result indicates that the two data  
671 sets form distinct statistical populations. Furthermore, Small and Fabel (2016b) happened to  
672 acquire their sample RMOOR04 from the same boulder surface as our sample RM-10-08 (see  
673 Figs. 1 and 5; and Table 1 for boulder coordinates), thus permitting a true interlaboratory  
674 comparison. Small and Fabel (2016b) reported a [ $^{10}\text{Be}$ ] for RMOOR04 of  $6.65 \pm 0.17$  [ $\times 10^4$ ] at  $\text{g}^{-1}$ .  
675 This value is 5.8% lower than that reported here from sample RM-10-08 for the same rock  
676 surface ( $7.06 \pm 0.21$  [ $\times 10^4$ ] at  $\text{g}^{-1}$ ; this study). When corrected for sample thickness, the  
677 difference is 5.5%. In either case, the magnitude of the offset exceeds the analytical  
678 uncertainties of each measurement. In light of this comparison, we consider that the source of

679 the offset between the two data sets is somehow related to the  $^{10}\text{Be}$  concentration data, and  
680 not due to sample selection.

681 At this time, the source of the offset between the Small and Fabel (2016b) data set and  
682 the data presented here is unclear. However, we can confirm that the  $^{10}\text{Be}$  data in this study  
683 were generated in a manner that is internally consistent (i.e., same methods, same laboratory,  
684 same accelerator, and all relative to the same 07KNSTD AMS standard), and thus should be  
685 directly comparable with several other primary geological calibration data sets (e.g., Kaplan et  
686 al., 2011; Kelly et al., 2015; Putnam et al., 2010b; Young et al., 2013). This apparent offset in  
687 reported  $^{10}\text{Be}$  measurements highlights the value of interlaboratory comparison (Jull et al.,  
688 2015). Therefore, to get to the bottom of the noted discrepancy in reported  $^{10}\text{Be}$   
689 measurements from Rannoch Moor, we are now coordinating a collaborative inter-laboratory  
690 comparison between LDEO/CAMS and the Scottish Universities Environmental Research Centre  
691 (SUERC) AMS laboratories (D. Fabel, personal communication, 06 August 2018).

692

## 693 7.0 Conclusions

694

- 695 1) We present a geological  $^{10}\text{Be}$  production-rate calibration based on the Rannoch Moor  
696 moraine belt of the central Scottish Highlands (56.63°N, 4.77°W; ~310—330 m a.s.l.).
- 697 2) The landforms targeted for production-rate calibration are bracketed by twenty-seven  
698 maximum- and twenty minimum-limiting  $^{14}\text{C}$  ages. This  $^{14}\text{C}$  chronology indicates that the  
699 Rannoch Moor moraines were formed no earlier than  $12,700 \pm 100$  cal. yrs BP, and no  
700 later than  $12,480 \pm 110$  cal. yrs BP. On the basis of these bracketing ages, we assigned a

701 midpoint age of  $12,590 \pm 140$  cal. yrs BP for when the Rannoch Moor moraines were  
702 constructed, and hence when the sampled boulders commenced their exposure to the  
703 cosmic-ray flux.

704 3) We measured  $^{10}\text{Be}$  concentrations from the surfaces of twelve boulders rooted in the  
705 Rannoch Moor moraine belt. The samples yield an arithmetic mean  $^{10}\text{Be}$  concentration  
706 ( $\pm 1\text{s}$ ) of  $6.93 \pm 0.23$  [ $\times 10^4$ ] atoms  $\text{g}^{-1}$  ( $N = 11$ ) after pruning one anomalously high  $^{10}\text{Be}$   
707 concentration (RM-10-01;  $7.70 \pm 0.15$  [ $\times 10^4$ ] at  $\text{g}^{-1}$ ). Together, the  $^{14}\text{C}$  chronology and  
708  $^{10}\text{Be}$  measurements from Rannoch Moor moraine boulders yields a local site-specific  
709 total  $^{10}\text{Be}$  production rate of  $5.50 \pm 0.18$  at  $\text{g}^{-1} \text{yr}^{-1}$  (i.e., including production both by  
710 muons and neutrons).

711 4) We used the calibration data set from Rannoch Moor with Version 3 of the UW online  
712 production-rate calculator to determine reference SLHL production rates [for neutron  
713 spallation only; muon-produced  $^{10}\text{Be}$  subtracted according to Balco (2017)] of  $3.91 \pm$   
714  $0.11$  and  $3.92 \pm 0.11$  at  $\text{g}^{-1} \text{yr}^{-1}$  using the 'St' and 'Lm' scaling models, respectively, and a  
715 production-rate correction factor of  $0.780 \pm 0.022$  at  $\text{g}^{-1} \text{yr}^{-1}$  using the 'LSDn' model. To  
716 facilitate comparison among production rates determined from elsewhere, we  
717 recalculated all far-field calibration data consistently using these methods.

718 5) The SLHL reference production rates presented here agree well with other widely  
719 distributed calibration data sets that are also based on landforms with direct and  
720 independent chronological control.

721 6) The resulting reference  $^{10}\text{Be}$  production-rate values from Rannoch Moor are 5–8% lower  
722 than those determined using the primary global calibration data set presented in

723 Borchers et al. (2016). In other words, applying the primary global  $^{10}\text{Be}$  production-rate  
724 calibration would yield Rannoch Moor exposure ages that are 2–5% younger than, and  
725 hence do not agree with, the independent minimum-limiting  $^{14}\text{C}$  chronology. The  $^{10}\text{Be}$   
726 production rates are also lower than the three previously published  $^{10}\text{Be}$  production-  
727 rate values from Scotland. We consider the hypothesis that the primary global  
728 calibration data set is biased toward those earlier Scottish studies that are based on  
729 landforms that do not have direct chronological control, but are instead tuned to distal  
730 proxy records. The  $^{10}\text{Be}$  production-rate data from Rannoch Moor, presented here,  
731 resolves these discrepancies by producing surface-exposure ages that accord with local  
732  $^{14}\text{C}$  chronologies.

733 7) Overall, the production-rate-calibration data set presented here can be used in  
734 conjunction with the UW online calculators for generating surface-exposure data sets  
735 for the British Isles, and perhaps farther afield, that are compatible with independent  
736  $^{14}\text{C}$  chronologies.

737

738 Acknowledgements: The authors wish to thank M.R. Kaplan, G.H. Denton, B.L. Hall, T.V. Lowell,  
739 J. Stone, C. Fenton, and many others for insightful discussions over the years. In particular, we  
740 are grateful to G. Balco for sharing his knowledge and providing advice on the technical aspects  
741 of production-rate calculation. G. Balco's 'cosmognosis' blog has also been very helpful. D.  
742 Fabel and D. Small provided helpful discussion regarding  $^{10}\text{Be}$  data from Rannoch Moor. M.  
743 Kelly and R. Braucher provided constructive comments that improved the paper. We  
744 acknowledge support from the Dan and Betty Churchill Exploration Fund and the Lamont-

745 Doherty Earth Observatory (LDEO) Climate Center. A.E.P and G.R.M.B. each acknowledge  
746 support from the LDEO Postdoctoral Fellowship. A.E.P. acknowledges the Lenfest Foundation,  
747 the Comer Family Foundation, and the Quesada Family Fund. J.M.S. acknowledges support  
748 from the Lamont Climate Center. We thank R. Schwartz and J. Frisch for assistance in the  
749 laboratory, as well as D. Duerden, E. Watson, and H. Senn for their help during field work at  
750 Rannoch Moor. This is LDEO contribution number XXXX.

751

752 Data Availability: Datasets related to this article can be found at [ENTER DOI HERE], an open-  
753 source online data repository hosted at Mendeley Data (Putnam et al., 2018).

754

755 References:

756

757 Balco, G., 2011. Contributions and unrealized potential contributions of cosmogenic-nuclide  
758 exposure dating to glacier chronology, 1990-2010. *Quaternary Science Reviews* 30, 3-27.

759 Balco, G., 2017. Production rate calculations for cosmic-ray-muon-produced  $^{10}\text{Be}$  and  $^{26}\text{Al}$   
760 benchmarked against geological calibration data. *Quaternary Geochronology* 39, 150-173.

761 Balco, G., 2018. ICE-D: Informal cosmogenic nuclide exposure-age database. Production-rate  
762 calibration data. <http://calibration.ice-d.org>.

763 Balco, G., Briner, J.P., Finkel, R., Rayburn, J.A., Ridge, J.C., Schaefer, J.M., 2009. Regional  
764 beryllium-10 production rate calibration for late-glacial northeastern North America.  
765 *Quaternary Geochronology* 4, 93-107.

766 Balco, G., Schaefer, J.M., 2006. Cosmogenic-nuclide and varve chronologies for the deglaciation  
767 of southern New England. *Quaternary Geochronology* 1, 15-28.

768 Balco, G., Stone, J.O., Lifton, N.A., Dunai, T.J., 2008. A complete and easily accessible means of  
769 calculating surface exposure ages or erosion rates from  $^{10}\text{Be}$  and  $^{26}\text{Al}$  measurements.  
770 *Quaternary Geochronology* 4, 93-107.

771 Ballantyne, C.K., Stone, J.O., 2012. Did large ice caps persist on low ground in north-west  
772 Scotland during the Lateglacial Interstade? *Journal of Quaternary Science* 27, 297-306.

- 773 Bevington, P., Robinson, D., 1992. Data Reduction and Error Analysis for the Physical Sciences.  
774 WCB McGraw Hill.
- 775 Bondevik, S., Mangerud, J., Birks, H.H., Gulliksen, S., Reimer, P., 2006. Changes in North Atlantic  
776 Radiocarbon Reservoir Ages During the Allerød and Younger Dryas. *Science* 312, 1514-1517.
- 777 Borchers, B., Marrero, S., Balco, G., Caffee, M., Goehring, B., Lifton, N., Nishiizumi, K., Phillips,  
778 F., Schaefer, J., Stone, J., 2016. Geological calibration of spallation production rates in the  
779 CRONUS-Earth project. *Quaternary Geochronology* 31, 188-198.
- 780 Braucher, R., Bourlès, D., Merchel, S., Vidal Romani, J., Fernandez-Mosquera, D., Marti, K.,  
781 Léanni, L., Chauvet, F., Arnold, M., Aumaître, G., Keddadouche, K., 2013. Determination of  
782 muon attenuation lengths in depth profiles from in situ produced cosmogenic nuclides. *Nuclear*  
783 *Instruments and Methods in Physics Research Section B: Beam Interactions with Materials and*  
784 *Atoms* 294, 484-490.
- 785 Broecker, W.S., 2006. Abrupt climate change revisited. *Global and Planetary Change* 54, 211-  
786 215.
- 787 Bromley, G., Putnam, A., Borns, H., Lowell, T., Sandford, T., Barrell, D., 2018. Interstadial Rise  
788 and Younger Dryas Demise of Scotland's Last Ice Fields. *Paleoceanography and*  
789 *Paleoclimatology* 33, 412-429.
- 790 Bromley, G.R.M., Putnam, A.E., Lowell, T.V., Hall, B.L., Schaefer, J.M., 2016. Comment on 'Was  
791 Scotland deglaciated during the Younger Dryas?' by Small and Fabel (2016). *Quaternary Science*  
792 *Reviews* 152, 203-206.
- 793 Bromley, G.R.M., Putnam, A.E., Rademaker, K.M., Lowell, T.V., Schaefer, J.M., Hall, B.L.,  
794 Winckler, G., Birkel, S.D., Borns, H.W., 2014. Younger Dryas deglaciation of Scotland driven by  
795 warming summers. *Proceedings of the National Academy of Sciences* 111, 6215-6219.
- 796 Browne, M.A.E., Graham, D.K., 1981. Glaciomarine deposits of the Loch Lomond Stade glacier in  
797 the Vale of Leven between Dumbarton and Balloch, west-central Scotland. *Quaternary*  
798 *Newsletter* 34, 1-7.
- 799 Browne, M.A.E., McMillan, A.A., Hall, I.H.S., 1983. Blocks of marine clay in till near Helensburgh,  
800 Strathclyde. *Scottish Journal of Geology* 19, 321-325.
- 801 Buizert, C., Gkinis, V., Severinghaus, J.P., He, F., Lacavalier, B.S., Kindler, P., Leuenberger, M.,  
802 Carlson, A.E., Vinther, B., Masson-Delmotte, V., White, J.W.C., Liu, Z., Otto-Bliesner, B., Brook,  
803 E.J., 2014. Greenland temperature response to climate forcing during the last deglaciation.  
804 *Science* 345, 1177-1180.
- 805 Chmeleff, J., von Blanckenburg, F., Kossert, K., Jakob, D., 2010. Determination of the <sup>10</sup>Be half-  
806 life by multicollector ICP-MS and liquid scintillation counting. *Nuclear Instruments and Methods*  
807 *in Physics Research Section B: Beam Interactions with Materials and Atoms* 268, 192-199.

808 Claude, A., Ivy-Ochs, S., Kober, F., Antognini, M., Salcher, B., Kubik, P.W., 2014. The Chironico  
809 Landslide (Valle Leventina, southern Swiss Alps): age and evolution. *Swiss Journal of*  
810 *Geoscience*, doi 10.1007/s000015-000014-000170-z.

811 Denton, G.H., Alley, R.B., Comer, G.C., Broecker, W.S., 2005. The role of seasonality in abrupt  
812 climate change. *Quaternary Science Reviews* 24, 1159-1182.

813 Goehring, B.M., Kurz, M.D., Balco, G., Schaefer, J.M., Licciardi, J.M., Lifton, N., 2010. A  
814 reevaluation of in situ cosmogenic <sup>3</sup>He production rates. *Quaternary Geochronology*  
815 doi:10.1016/j.quageo.2010.03.001.

816 Goehring, B.M., Lohne, Ø.S., Mangerud, J., Svendsen, J.I., Gyllencreutz, R., Schaefer, J.M., Finkel,  
817 R., 2012. Late Glacial and Holocene <sup>10</sup>Be production rates for western Norway. *Journal of*  
818 *Quaternary Science* 27, 89-96.

819  
820 Golledge, N.R., 2007. An ice cap landsystem for palaeoglaciological reconstructions:  
821 characterizing the Younger Dryas in western Scotland. *Quaternary Science Reviews* 26, 213-229.

822 Golledge, N.R., 2010. Glaciation of Scotland during the Younger Dryas stadial: a review. *Journal*  
823 *of Quaternary Science* 25, 550-566.

824 Golledge, N.R., Fabel, D., Everest, J.D., Freeman, S., Binnie, S., 2007. First cosmogenic <sup>10</sup>Be age  
825 constraint on the timing of Younger Dryas glaciation and ice cap thickness, western Scottish  
826 Highlands. *Journal of Quaternary Science* 22, 785-791.

827 Gray, J.M., Brooks, C.L., 1972. The Loch Lomond Readvance moraines of Mull and Menteith.  
828 *Scottish Journal of Geology* 8, 95-103.

829 Heisinger, B., Lal, D., Jull, A.J.T., Kubik, P., Ivy-Ochs, S., Knie, K., Nolte, E., 2002a. Production of  
830 selected cosmogenic radionuclides by muons: 2. Capture of negative muons. *Earth and*  
831 *Planetary Science Letters* 200, 357-369.

832 Heisinger, B., Lal, D., Jull, A.J.T., Kubik, P., Ivy-Ochs, S., Neumaier, S., Knie, K., Lazarev, V., Nolte,  
833 E., 2002b. Production of selected cosmogenic radionuclides by muons: 1. Fast muons. *Earth and*  
834 *Planetary Science Letters* 200, 345-355.

835 Heyman, J., 2014. Paleoglaciation of the Tibetan Plateau and surrounding mountains based on  
836 exposure ages and ELA depression estimates. *Quaternary Science Reviews* 91, 30-41.

837 Jull, A.J.T., Scott, E.M., Bierman, P., 2015. The CRONUS-Earth inter-comparison for cosmogenic  
838 isotope analysis. *Quaternary Geochronology* 26, 3-10.

839 Kaplan, M.R., Strelin, J.A., Schaefer, J.M., Denton, G.H., Finkel, R.C., Schwartz, R., Putnam, A.E.,  
840 Vandergoes, M.J., Goehring, B.M., Travis, S.G., 2011. In-situ cosmogenic <sup>10</sup>Be production rate at  
841 Lago Argentino, Patagonia: Implications for late-glacial climate chronology. *Earth and Planetary*  
842 *Science Letters* 309, 21-32.

843 Kelly, M.A., 2003. The Late Würmian Age in the western Swiss Alps - Last glacial maximum  
844 (LGM) ice-surface reconstruction and  $^{10}\text{Be}$  dating of late-glacial features. University of Bern, p.  
845 105.

846 Kelly, M.A., Lowell, T.V., Applegate, P.J., Phillips, F.M., Schaefer, J.M., Smith, C.A., Kim, H.,  
847 Leonard, K.C., Hudson, A.M., 2015. A locally calibrated, late glacial  $^{10}\text{Be}$  production rate from a  
848 low-latitude, high-altitude site in the Peruvian Andes. *Quaternary Geochronology* 26, 70-85.

849 Kohl, C.P., Nishiizumi, K., 1992. Chemical isolation of quartz for measurement of in-situ -  
850 produced cosmogenic nuclides. *Geochimica et Cosmochimica Acta* 56, 3583-3587.

851 Korschinek, G., Bergmaier, A., Dillmann, I., Faestermann, T., Gerstmann, U., Knie, K., von  
852 Gostomski, C.L., Maiti, M., Poutivtsev, M., Remmert, A., Rugel, G., Wallner, A., 2009.  
853 Determination of the  $^{10}\text{Be}$  half-life by HI-IRD and liquid scintillation counting. *Geochimica Et*  
854 *Cosmochimica Acta* 73, A685.

855 Lal, D., 1991. Cosmic-ray labeling of erosion surfaces: in situ nuclide production rates and  
856 erosion models. *Earth and Planetary Science Letters* 104, 424-439.

857 Lambeck, K., 1991. Glacial rebound and sea-level change in the British Isles. *Terra Nova* 3, 379-  
858 389.

859 Lifton, N., Bieber, J., Clem, J., Duldig, M., Evenson, P., Humble, J., Pyle, R., 2005. Addressing  
860 solar modulation and long-term uncertainties in scaling secondary cosmic rays for in situ  
861 cosmogenic nuclide applications. *Earth and Planetary Science Letters* 239, 140-161.

862 Lifton, N., Sato, T., Dunai, T.J., 2014. Scaling in situ cosmogenic nuclide production rates using  
863 analytical approximations to atmospheric cosmic-ray fluxes. *Earth and Planetary Science Letters*  
864 386, 149-160.

865 Lifton, N., Smart, B., Shea, M., 2008. Scaling time-integrated in situ cosmogenic nuclide  
866 production rates using a continuous geomagnetic model. *Earth and Planetary Science Letters*  
867 268, 190-201.

868 Lowe, J.J., 1982. Three Flandrian pollen profiles from the Teith valley, Perthshire, Scotland. *New*  
869 *Phytologist* 90, 371-385.

870 Lowe, J.J., Walker, M.J.C., 1976. Radiocarbon dates and deglaciation of Rannoch Moor,  
871 Scotland. *Nature* 264, 632.

872 Mackintosh, A.N., Anderson, B.M., Pierrehumbert, R.T., 2017. Reconstructing Climate from  
873 Glaciers. *Annual Review of Earth and Planetary Sciences* 45, 649-680.  
874

875 MacLeod, A., Matthews, I.P., Lowe, J.J., Palmer, A.P., Albert, P.G., 2015. A second tephra  
876 isochron for the Younger Dryas period in northern Europe: The Abernethy Tephra. *Quaternary*  
877 *Geochronology* 28, 1-11.

878 Martin, L.C.P., Blard, P.-H., Lavé, J., Braucher, R., Lupker, M., Condom, T., Charreau, J., Mariotti,  
879 V., A.S.T.E.R. Team, Davy, E., 2015. In situ  $^{10}\text{Be}$  production rate in the High Tropical Andes.  
880 Quaternary Geochronology 30A, 54-68.

881 Nishiizumi, K., Imamura, M., Caffee, M.W., Southon, J.R., Finkel, R.C., McAninch, J., 2007.  
882 Absolute calibration of  $^{10}\text{Be}$  AMS standards. Nuclear Instruments and Methods in Physics  
883 Research B 258, 403-413.

884 Oerlemans, J., 2005. Extracting a Climate Signal from 169 Glacier Records. Science 308, 675-  
885 677.

886  
887 Ordnance Survey, 2015. Rannoch Moor & Ben Alder, sheet 385. Ordnance Survey (Explorer  
888 Series), Southampton.

889 Palmer, A.P., Rose, J., Lowe, J.J., MacLeod, A., 2010. Annually resolved events of Younger Dryas  
890 glaciation in Lochaber (Glen Roy and Glen Spean), western Scottish Highlands. Journal of  
891 Quaternary Science 25, 581-596.

892 Peacock, J.D., 1971. Marine Shell Radiocarbon Dates and the Chronology of Deglaciation in  
893 Western Scotland. Nature Physical Science 230, 43.

894 Phillips, F.M., 2015. Preface – The CRONUS-EARTH Volume. Quaternary Geochronology 26, 1-2.

895 Phillips, F.M., Argento, D.C., Balco, G., Caffee, M.W., Clem, J., Dunai, T.J., Finkel, R., Goehring,  
896 B., Gosse, J.C., Hudson, A.M., Jull, A.J.T., Kelly, M.A., Kurz, M., Lal, D., Lifton, N., Marrero, S.M.,  
897 Nishiizumi, K., Reedy, R.C., Schaefer, J., Stone, J.O.H., Swanson, T., Zreda, M.G., 2016. The  
898 CRONUS-Earth Project: A synthesis. Quaternary Geochronology 31, 119-154.

899 Pigati, J.S., Lifton, N.A., 2004. Geomagnetic effects on time-integrated cosmogenic nuclide  
900 production with emphasis on in situ  $^{14}\text{C}$  and  $^{10}\text{Be}$ . Earth and Planetary Science Letters 226, 193-  
901 205.

902 Putnam, A.E., Denton, G.H., Schaefer, J.M., Barrell, D.J.A., Andersen, B.G., Finkel, R., Schwartz,  
903 R., Doughty, A.M., Kaplan, M., Schlüchter, C., 2010a. Glacier advance in southern middle  
904 latitudes during the Antarctic Cold Reversal. Nature Geoscience 3, 700-704.

905 Putnam, A.E., Schaefer, J.M., Barrell, D.J.A., Vandergoes, M., Denton, G.H., Kaplan, M.R.,  
906 Schwartz, R., Finkel, R.C., Goehring, B.M., Kelley, S.E., 2010b. In situ cosmogenic  $^{10}\text{Be}$   
907 production-rate calibration from the Southern Alps, New Zealand. Quaternary Geochronology  
908 5, 392-409.

909 Rasmussen, S.O., Andersen, K.K., Svensson, A.M., Steffensen, J.P., Vinther, B.M., Clausen, H.B.,  
910 Siggaard-Andersen, M.-L., Johnsen, S.J., Larsen, L.B., Dahl-Jensen, D., Bigler, M., Röthlisberger,  
911 R., Fischer, H., Goto-Azuma, K., Hansson, M.E., Ruth, U., 2006. A new Greenland ice core  
912 chronology for the last glacial termination. Journal of Geophysical Research 111, D06102.

913 Reimer, P.J., Bard, E., Bayliss, A., Beck, J.W., Blackwell, P.G., Bronk Ramsay, C., Buck, C.E.,  
914 Cheng, H., Edwards, R.L., Friedrich, M., Grootes, P., Guilderson, T.P., Hafliðason, H., Hajdas, I.,  
915 Hatté, C., Heaton, T.J., Hoffmann, D.L., Hogg, A.G., Hughen, K.A., Kaiser, K.F., Kromer, B.,  
916 Manning, S.W., Niu, M., Reimer, R.W., Richards, D.A., Scott, E.M., Southon, J.R., Staff, R.A.,  
917 Turney, C.S.M., van der Plicht, J., 2013. INTCAL13 and MARINE13 radiocarbon age calibration  
918 curves 0-50,000 years cal BP. *Radiocarbon* 55, 1869-1887.

919 Rose, J., 1980. Quaternary Research Association Glasgow Region field guide (pp. 25-37).  
920 Quaternary Research Association, Cambridge.

921 Rupper, S., Roe, G., 2008. Glacier changes and regional climate: A mass and energy balance  
922 approach. *Journal of Climate* 21, 5384-5401.

923  
924 Schaefer, J.M., Denton, G.H., Kaplan, M., Putnam, A., Finkel, R.C., Barrell, D.J.A., Andersen, B.G.,  
925 Schwartz, R., Mackintosh, A., Chinn, T., Schlüchter, C., 2009. High-frequency Holocene glacier  
926 fluctuations in New Zealand differ from the northern signature. *Science* 324, 622-625.

927 Schenk, F., Väliranta, M., Muschitiello, F., Tarasov, L., Heikkilä, M., Björck, S., Brandefelt, J.,  
928 Johansson, A.V., Näslund, J.-O., Wohlfarth, B., 2018. Warm summers during the Younger Dryas  
929 cold reversal. *Nature Communications* 9, 1634.

930 Sissons, J.B., 1967. Glacial stages and radiocarbon dates in Scotland. *Scottish Journal of Geology*  
931 3, 375-381.

932 Sissons, J.B., 1976. *The Geomorphology of the British Isles: Scotland*. Methuen, London.

933 Sissons, J.B., 1978. The parallel roads of Glen Roy and adjacent glens, Scotland. *Boreas* 7, 229-  
934 244.

935 Small, D., Fabel, D., 2015. A Lateglacial <sup>10</sup>Be production rate from glacial lake shorelines in  
936 Scotland. *Journal of Quaternary Science* 30, 509-513.

937 Small, D., Fabel, D., 2016a. Response to Bromley et al. "Comment on 'Was Scotland deglaciated  
938 during the Younger Dryas?' By Small and Fabel (2016)". *Quaternary Science Reviews* 152, 206-  
939 208.

940 Small, D., Fabel, D., 2016b. Was Scotland deglaciated during the Younger Dryas? *Quaternary*  
941 *Science Reviews* 145, 259-263.

942 Stockamp, J., Bishop, P., Li, Z., Petrie, E.J., Hansom, J., Rennie, A., 2016. State-of-the-art in  
943 studies of glacial isostatic adjustment for the British Isles: a literature review. *Earth and*  
944 *Environmental Science Transactions of the Royal Society of Edinburgh* 106, 145-170.

945 Stone, J.O., 2000. Air pressure and cosmogenic isotope production. *Journal of Geophysical*  
946 *Research* 105, 23753-23759.

- 947 Stone, J.O., Ballantyne, C.K., Keith Fifield, L., 1998. Exposure dating and validation of periglacial  
948 weathering limits, northwest Scotland. *Geology* 26, 587-590.
- 949 Strelin, J.A., Denton, G.H., Vandergoes, M.J., Ninnemann, U.S., Putnam, A.E., 2011. Radiocarbon  
950 chronology of the late-glacial Puerto Bandera moraines, Southern Patagonian Icefield,  
951 Argentina. *Quaternary Science Reviews* 30, 2551-2569.
- 952 Stroeven, A.P., Heyman, J., Fabel, D., Björck, S., Caffee, M.W., Fredin, O., Harbor, J.M., 2015. A  
953 new Scandinavian reference  $^{10}\text{Be}$  production rate. *Quaternary Geochronology* 29, 104-115.  
954
- 955 Thorp, P.W., 1984. The glacial geomorphology of part of the western Grampians of Scotland  
956 with especial reference to the limits of the Loch Lomond Advance. City of London Polytechnic.
- 957 Thorp, P.W., 1986. A mountain icefield of Loch Lomond Stadial age, western Grampians,  
958 Scotland. *Boreas* 15, 83-97.
- 959 Uppala, S.M., Kållberg, P.W., Simmons, A.J., Andrae, U., Bechtold, V.D.C., Fiorino, M., Gibson,  
960 J.K., Haseler, J., Hernandez, A., Kelly, G.A., Li, X., Onogi, K., Saarinen, S., Sokka, N., Allan, R.P.,  
961 Andersson, E., Arpe, K., Balmaseda, M.A., Beljaars, A.C.M., Berg, L.V.D., Bidlot, J., Bormann, N.,  
962 Caires, S., Chevallier, F., Dethof, A., Dragosavac, M., Fisher, M., Fuentes, M., Hagemann, S.,  
963 Hólm, E., Hoskins, B.J., Isaksen, I., Janssen, P.A.E.M., Jenne, R., McNally, A.P., Mahfouf, J.F.,  
964 Morcrette, J.J., Rayner, N.A., Saunders, R.W., Simon, P., Sterl, A., Trenberth, K.E., Untch, A.,  
965 Vasiljevic, D., Viterbo, P., Woollen, J., 2005. The ERA-40 re-analysis. *Quarterly Journal of the*  
966 *Royal Meteorological Society* 131, 2961-3012.
- 967 Walker, M.J.C., Lowe, J.J., 1977. Postglacial Environmental History of Rannoch Moor, Scotland. I.  
968 Three Pollen Diagrams from the Kingshouse Area. *Journal of Biogeography* 4, 333-351.
- 969 Walker, M.J.C., Lowe, J.J., 1982. Lateglacial and early Flandrian chronology of the Isle of Mull,  
970 Scotland. *Nature* 296, 558.
- 971 Walker, M.J.C., Lowe, J.J., 1979. Postglacial Environmental History of Rannoch Moor, Scotland.  
972 II. Pollen Diagrams and Radiocarbon Dates from the Rannoch Station and Corrou Area. *Journal*  
973 *of Biogeography* 6, 349-362.
- 974 Young, N.E., Schaefer, J.M., Briner, J.P., Goehring, B.M., 2013. A  $^{10}\text{Be}$  production-rate calibration  
975 for the Arctic. *Journal of Quaternary Science* 28, 515-526.  
976
- 977 Zemp, M., Frey, H., Gärtner-Roer, I., Nussbaumer, S.U., Hoelzle, M., Paul, F., Haeberli, W.,  
978 Denzinger, F., Ahlstrøm, A.P., Anderson, B., Bajracharya, S., Baroni, C., Braun, L.N., Cáceres, B.E.,  
979 Casassa, G., Cobos, G., Dávila, L.R., Delgado Granados, H., Demuth, M.N., Espizua, L., Fischer, A.,  
980 Fujita, K., Gadek, B., Ghazanfar, A., Hagen, J.O., Holmlund, P., Karimi, N., Li, Z., Pelto, M., Pitte,  
981 P., Popovnin, V.V., Portocarrero, C.A., Prinz, R., Sangewar, C.V., Severskiy, I., Sigurðsson, O.,  
982 Soruco, A., Usabaliev, R., Vincent, C., 2015. Historically unprecedented global glacier decline in  
983 the early 21st century. *Journal of Glaciology* 61, 745-762.



985 Figure captions.

986 **Figure 1.** Geographic and glacial-geomorphic setting of the Rannoch Moor  $^{10}\text{Be}$  calibration site.  
987 **A)** Distribution of moraine ridges on Rannoch Moor and locations (red circles) of sediment  
988 cores, along with respective basal  $^{14}\text{C}$  ages. Radiocarbon dates are shown as calibrated ages,  
989 with the closest limiting minimum ages for deglaciation in bold. Topographic contours are  
990 shown in grey (interval = 100 m). **B)** Position of Rannoch Moor in Scotland and estimated extent  
991 of the WHIF. **C)** Zoomed-in view of the Rannoch Moor moraine belt, indicating the locations of  
992 boulders sampled for cosmogenic  $^{10}\text{Be}$  measurement (blue circles: this study; yellow circles:  
993 Small and Fabel, (2016b)). Sediment core sites denoted by red circles correspond to those  
994 shown in Panel A. Adapted from Fig. 2 in Bromley et al. (2014).

995  
996 **Figure 2.** Former extent of the southern WHIF and the radiocarbon chronology (in kcal yr B.P.)  
997 used to bracket its maximum extent. Also shown is the former Mull ice field (MIF). Blue circles  
998 represent the locations of maximum-limiting  $^{14}\text{C}$  ages, while red circles indicate the locations of  
999 minimum-limiting ages. Minimum ages from Rannoch Moor include the five oldest basal ages  
1000 reported by Bromley et al. (2014) (asterisk) together with those published earlier by Walker &  
1001 Lowe (1979). Adapted from Fig. 1 of Bromley et al. (2018).

1002  
1003 **Figure 3.** Panorama of the Rannoch Moor moraine belt. Vantage is to the east. The boulder-  
1004 mantled sub-parallel moraine ridges are featured in the center of the photograph.  
1005 Intermorainal depressions were the targets for coring described in Bromley et al. (2014).

1006  
1007 **Figure 4.** Probability distribution functions for minimum- and maximum-limiting  $^{14}\text{C}$   
1008 populations, converted to calendar years, bracketing the latest culmination of the WHIF. The  
1009 most probable age for the maximum extent of the WHIF, which serves as a maximum age for  
1010 the Rannoch Moor moraines in this study, was calculated using a PDF (not shown) of the  
1011 interval between the two populations. Vertical black line and yellow shading represent the  
1012 mean age and  $1\sigma$  uncertainty, respectively, of the Rannoch Moor beryllium ages ( $n = 11$ )  
1013 calculated with our production rate. Adapted from Fig. 3 of Bromley et al. (2018)

1014  
1015 **Figure 5.** Photographs of boulders in the Rannoch Moor field area selected for  $^{10}\text{Be}$  sample  
1016 collection. Sample information is given in Table 2.

1017  
1018 **Figure 6.** Camel plot of measured  $^{10}\text{Be}$  concentrations from the Rannoch Moor boulders.  
1019 Concentrations have been corrected for thickness and topographic shielding, but not for  
1020 differences in sample elevations. Thin, solid curves are Gaussian approximations of individual  
1021  $^{10}\text{Be}$  analyses (given in Table 2). The thick solid curve represents the summed probability of the  
1022 distribution. Thin, dashed line represents an anomalously high  $^{10}\text{Be}$  concentration that is  
1023 considered an outlier and excluded from further consideration. Gray vertical band represents  
1024 the  $1\sigma$  uncertainty of the distribution. Yellow vertical band represents the standard error of the  
1025 mean. The vertical blue line denotes the arithmetic mean value of the distribution. Statistics are  
1026 inset.

1027

1028 **Figure 7.** Comparison of Rannoch Moor production rates and correction factors ( $P_{RM}$ ) with a set  
1029 of distal production-rate calibration data set for the 'St', 'Lm', and 'LSDn' scaling models. Values  
1030 are presented as ratios and normalized to the Rannoch Moor value. The vertical gray bands  
1031 represent the Rannoch Moor production-rate uncertainties. Abbreviations for selected  
1032 calibration data sets are as follows: 'PAT' = Patagonia (Kaplan et al., 2011), 'NZ' = New Zealand  
1033 (Putnam et al., 2010a), 'PERU1' = Peru (Kelly et al., 2015), 'PERU2' = Peru (Martin et al., 2015),  
1034 'NENA' = Northeast North America (Balco et al., 2009); 'SWISS' = Switzerland (Claude et al.,  
1035 2014), 'BB' = Baffin Bay (Young et al., 2013), and 'GLOBAL' = the primary global calibration data  
1036 set of Borchers et al. (2016).

1037  
1038 **Figure 8.** Comparison of Rannoch Moor  $^{10}\text{Be}$  data from this study (top) and from Small and  
1039 Fabel (2016b) (bottom).  $^{10}\text{Be}$  concentrations have been corrected for thickness and topographic  
1040 shielding, scaled to SLHL (using the 'St' scaling model), and normalized to the arithmetic mean  
1041 value of the data reported in this study. We note that the observed offset in  $^{10}\text{Be}$  distributions  
1042 is independent of choice of scaling model used to correct for differences in boulder-sample  
1043 elevations. Thin black curves are Gaussian approximations of individual sample analyses. Thick  
1044 black lines are summed probability curves for each distribution. Thin, dashed lines are Gaussian  
1045 representations of samples with anomalously high concentrations (treated as outliers). Vertical  
1046 gray bands represent  $1\sigma$  uncertainties for each distribution. Yellow bands represent the  
1047 standard error of the mean for each distribution. Vertical blue lines correspond to arithmetic  
1048 means for each distribution. Bold red lines refer to the Gaussian representations of samples  
1049 RM-10-08 (top) and RMOOR04 (bottom), which were each collected from the same boulder  
1050 surface. Note that the overall distributions are offset by  $\sim 7.9\%$ . RM-10-08 and RMOOR04,  
1051 collected from the same rock surface, exhibit an offset of  $\sim 5.5\%$ .

1052

1053 Tables

1054

1055 Table 1. <sup>14</sup>C data. Minimum-limiting data are shaded tan. Maximum-limiting data are shaded blue.

Core/Site	AMS no.	Latitude (°)	Longitude (°)	<sup>14</sup> C age (yr)	Calendar age (yr BP)	δ <sup>13</sup> C	Type	Context	Reference	Notes
RM-10-1A	OS-93723	56.6338 N	4.7714 W	10,100 ± 35	11,701 ± 123	-28.0	Beetle	Minimum	Bromley et al., 2014	Ages in this group are all from samples recovered from the lowermost sediments of Rannoch Moor bogs (Bromley et al., 2014). Asterisks denote replicate samples from respective cores. Bold indicates the 5 oldest samples used to provide minimum ages for deglaciation of Rannoch Moor in the Bromley et al. (2014) paper.
RM-10-1C	OS-84320	56.6338 N	4.7714 W	10,200 ± 80	11,885 ± 176	-22.7	Pogonatum, unidentified leaf fragments	Minimum	Bromley et al., 2014	
RM-10-1D	OS-89837	56.6338 N	4.7714 W	9980 ± 50	12,217 ± 103	-24.1	Sphagnum, Potamogeton, Betula leaf	Minimum	Bromley et al., 2014	
RM-10-3A	OS-9978*	56.6358 N	4.7763 W	<b>10,350 ± 40</b>	<b>12,217 ± 103</b>	<b>-20.0</b>	<b>Empetrum seed, Pogonatum, unidentified stem</b>	<b>Minimum</b>	<b>Bromley et al., 2014</b>	
RM-10-3A	OS-89842*	56.6358 N	4.7763 W	10,500 ± 50	12,446 ± 100	-21.7	Sphagnum, Pogonatum, unidentified leaf fragments	Minimum	Bromley et al., 2014	
RM-10-3A	OS-89841*	56.6358 N	4.7763 W	10,300 ± 70	12,120 ± 158	-23.5	Chara, Nitella, Potamogeton, Empetrum seed	Minimum	Bromley et al., 2014	
RM-10-3A	OS-9977*	56.6358 N	4.7763 W	10,400 ± 45	12,274 ± 105	-21.5	Empetrum seed, Pogonatum	Minimum	Bromley et al., 2014	
RM-12-1	112593	56.6565 N	4.7349 W	10,040 ± 40	11,547 ± 115	NR	Potamogeton, Pogonatum, unidentified stems	Minimum	Bromley et al., 2014	
RM-12-2A	OS-99684	56.6594 N	4.8039 W	10,050 ± 65	11,583 ± 158	-24.3	Sphagnum, Pogonatum, Potamogeton	Minimum	Bromley et al., 2014	
RM-12-2B	112598	56.6594 N	4.8039 W	9945 ± 20	11,332 ± 52	NR	Rhacomitrium, Pogonatum, Empetrum seed, unidentified bud	Minimum	Bromley et al., 2014	
RM-12-3A	OS-99685	<b>56.6367 N</b>	<b>4.7922 W</b>	<b>10,550 ± 65</b>	<b>12,481 ± 95</b>	<b>-25.7</b>	<b>Pogonatum, wood fragment, Betula leaf fragment</b>	<b>Minimum</b>	<b>Bromley et al., 2014</b>	
RM-12-3B	112603*	56.6367 N	4.7922 W	10,120 ± 170	11,760 ± 303	NR	Pogonatum, Vaccinium leaf fragments	Minimum	Bromley et al., 2014	
RM-12-3B	OS-100115*	56.6367 N	4.7922 W	10,100 ± 70	11,685 ± 174	-19.8	Unidentified leaf fragments	Minimum	Bromley et al., 2014	
RM-12-4A	112605*	56.6337 N	4.7714 W	9990 ± 20	11,449 ± 91	NR	Rhacomitrium	Minimum	Bromley et al., 2014	
RM-12-4A	112604*	56.6337 N	4.7714 W	9965 ± 20	11,375 ± 77	NR	Rhacomitrium	Minimum	Bromley et al., 2014	
RM-12-4B	OS-99686	56.6337 N	4.7714 W	10,050 ± 60	11,579 ± 151	-26.8	Rhacomitrium	Minimum	Bromley et al., 2014	
RM-12-5	112608	56.6355 N	4.7732 W	9140 ± 180	10,319 ± 267	NR	Nitella, Chara, Betula seed, Sphagnum, unidentified stems	Minimum	Bromley et al., 2014	
RM-13-3	OS-104748*	56.6594 N	4.8039 W	10,150 ± 35	11,836 ± 95	-25.1	Rhacomitrium	Minimum	Bromley et al., 2014	
RM-13-3	OS-104747*	56.6594 N	4.8039 W	10,100 ± 40	11,698 ± 133	-25.0	Rhacomitrium	Minimum	Bromley et al., 2014	
RM-13-3	OS-104746*	56.6594 N	4.8039 W	10,250 ± 85	11,999 ± 191	-23.6	Rhacomitrium	Minimum	Bromley et al., 2014	
Balloch	SRR-1530	56.0034 N	4.5850 W	11,320 ± 130	12,809 ± 246	NR	Barnacles	Minimum	Browne & Graham, 1981	Ages in this group include published marine and terrestrial samples that together afford minimum-limiting age control for the culmination of the WHIF (from Bromley et al., 2018). These data were used to generate the PDF calculation in Bromley et al. (2018). All marine ages converted using Marine13.
Balloch	OS-2078	56.0034 N	4.5850 W	11,050 ± 45	12,598 ± 93	-0.20	Portlandia arctica shell	Minimum	Bromley et al., 2018	
Mollands	HV-5647	56.2334 N	4.2164 W	10,670 ± 85	12,612 ± 78	NR	Gytija	Minimum	Lowe, 1978	
Mollands	HV-5646	56.2334 N	4.2164 W	10,480 ± 150	12,330 ± 220	NR	Fine detritus peat	Minimum	Lowe, 1978	
Torness	SRR-1797	56.4328 N	5.8246 W	10,170 ± 150	11,829 ± 292	NR	Gytija	Minimum	Walker & Lowe, 1982	
Rannoch Station 2	BIRM-858	56.6834 N	4.5809 W	10,390 ± 200	12,163 ± 317	-22.0	Gytija	Minimum	Walker & Lowe, 1979	
K2	BIRM-722	56.6594 N	4.8039 W	10,290 ± 180	12,031 ± 321	NR	Rhacomitrium	Minimum	Lowe & Walker, 1976	
K2	BIRM-723	56.6594 N	4.8039 W	10,520 ± 330	12,245 ± 442	-22.4	Gytija	Minimum	Lowe & Walker, 1976	
Kinlochspelve	AA15940	56.3687 N	5.7981 W	11,621 ± 117	13,096 ± 257	1.9	Astarte elliptica	Maximum	Bromley et al., 2018	Ages in this population include published marine samples that together afford maximum-limiting age control for the culmination of the WHIF (from Bromley et al., 2018). These data were used to generate the PDF in Bromley et al. (2018). All marine ages converted using Marine13.
Kinlochspelve	I-5308	56.3687 N	5.7981 W	11,330 ± 170	12,830 ± 315	NR	Unidentified shell fragments	Maximum	Gray & Brooks, 1972	
Loch Spelve	AA15941	56.3650 N	5.7856 W	12,167 ± 130	13,625 ± 281	1.6	Arctica Islandica	Maximum	Bromley et al., 2018	
Loch Spelve	AA15942	56.3650 N	5.7856 W	11,352 ± 92	12,824 ± 201	2.2	Astarte elliptica	Maximum	Bromley et al., 2018	
Loch Spelve	AA15943	56.3650 N	5.7856 W	11,668 ± 86	13,154 ± 202	0.1	Nuculana pernula	Maximum	Bromley et al., 2018	
South Shian	AA15945	56.5252 N	5.4018 W	11,192 ± 78	12,688 ± 141	1.9	Astarte elliptica	Maximum	Bromley et al., 2018	
South Shian	AA15946	56.5252 N	5.4018 W	12,157 ± 120	13,614 ± 262	2.5	Arctica Islandica	Maximum	Bromley et al., 2018	
South Shian	IGS C14/16	56.5252 N	5.4018 W	11,930 ± 210	13,400 ± 450	NR	Chlamys islandicus	Maximum	Peacock, 1971	
South Shian	IGS C14/17	56.5252 N	5.4018 W	12,205 ± 180	13,669 ± 375	NR	Astarte elliptica	Maximum	Peacock, 1971	
South Shian	IGS C14/18	56.5252 N	5.4018 W	11,830 ± 220	13,295 ± 468	NR	Unidentified shell fragments	Maximum	Peacock, 1971	
North Shian	AA15947	56.5345 N	5.3895 W	12,700 ± 116	14,326 ± 477	2.7	Arctica Islandica	Maximum	Bromley et al., 2018	
North Shian	AA15948	56.5345 N	5.3895 W	12,179 ± 85	13,632 ± 206	1.3	Unidentified shell fragments	Maximum	Bromley et al., 2018	
Furnace	OS-2077	56.1502 N	5.1882 W	11,450 ± 45	12,914 ± 206	1.4	Unidentified shell fragments	Maximum	Bromley et al., 2018	
Gartocharn	AA15951	56.0392 N	4.5290 W	12,021 ± 89	13,472 ± 202	0.1	Astarte elliptica	Maximum	Bromley et al., 2018	
Aber	AA15949	56.0564 N	4.5280 W	12,816 ± 86	14,518 ± 421	0.8	Unidentified shell fragments	Maximum	Bromley et al., 2018	
Aber	AA15950	56.0564 N	4.5280 W	12,528 ± 94	14,014 ± 250	0.6	Unidentified shell fragments	Maximum	Bromley et al., 2018	
Drumbeg	AA15952	56.0571 N	4.4378 W	12,021 ± 89	13,472 ± 202	-1.1	Unidentified shell fragments	Maximum	Bromley et al., 2018	
Drumbeg	OS-2076	56.0571 N	4.4378 W	12,250 ± 50	13,713 ± 167	3.2	Chlamys islandicus	Maximum	Bromley et al., 2018	
Gartness	AA15953	56.0401 N	4.4139 W	11,593 ± 79	13,072 ± 202	0.8	Unidentified shell fragments	Maximum	Bromley et al., 2018	
Gartness	OS-133096	56.0401 N	4.4139 W	12,650 ± 35	14,142 ± 150	0.6	Astarte borealis	Maximum	Bromley et al., 2018	
Menteith	AA15938	56.1717 N	4.2742 W	12,058 ± 89	13,511 ± 206	0.8	Mytilus edulis fragments	Maximum	Bromley et al., 2018	
Menteith	AA15939	56.1717 N	4.2742 W	11,843 ± 88	13,312 ± 203	3.0	Unidentified shell fragments	Maximum	Bromley et al., 2018	
Menteith	I-2234	56.1717 N	4.2742 W	11,800 ± 170	13,265 ± 371	NR	Unreported	Maximum	Sissons, 1967	
Drymen	I-2235	56.0607 N	4.4380 W	11,700 ± 170	13,165 ± 347	NR	Unreported	Maximum	Sissons, 1967	
Rhu Point	HAR-931	56.0163 N	4.7858 W	11,520 ± 250	13,001 ± 453	NR	Unreported	Maximum	Rose, 1980	
Helensburgh	SRR-2006	56.0092 N	4.7024 W	12,110 ± 60	13,559 ± 167	NR	Arctica Islandica	Maximum	Browne et al., 1983	
Helensburgh	NR	56.0092 N	4.7024 W	12,190 ± 60	13,642 ± 172	NR	Arctica Islandica	Maximum	Browne et al., 1983	

1056

1057 **Table 2.** Rannoch Moor boulder sample details and <sup>10</sup>Be data.

CAMS laboratory no.	Sample ID	Latitude (°)	Longitude (°)	Elevation (m a.s.l.)	Boulder size (L x W x H) (cm)	Sample Thickness (cm)	Shielding corr.	Quartz weight (g)	Carrier added (g)	Carrier conc. (ppm) <sup>d</sup>	<sup>10</sup> Be/ <sup>9</sup> Be ± 1s (10 <sup>-14</sup> ) <sup>b</sup>	[ <sup>10</sup> Be] ± 1s (10 <sup>1</sup> atoms g <sup>-1</sup> ) <sup>c</sup>	<sup>9</sup> Be current (μA) <sup>d</sup>	Blank	AMS Std
BE35521	RM-10-01	56.6334	-4.77118	316	210 x 150 x 68.75	0.93	1.000	25.0222	0.1850	1032	15.179 ± 0.28	7.70 ± 0.15	19.8 (74%)	B3, B4	07KNSTD
BE34648	RM-10-02	56.63338	-4.77133	316	220 x 130 x 86.25	2.23	1.000	20.0469	0.1832	1030	11.041 ± 0.25	6.94 ± 0.16	16.7 (72%)	B1, B2	07KNSTD
BE34649	RM-10-03	56.63369	-4.77312	321	190 x 170 x 87.5	0.75	1.000	20.0032	0.1839	1030	11.312 ± 0.23	7.15 ± 0.15	19.3 (84%)	B1, B2	07KNSTD
BE38226	RM-10-06	56.63377	-4.7766	325	150 x 140 x 101.25	0.67	1.000	15.0040	0.1808	1036	8.758 ± 0.17	7.30 ± 0.14	23.0 (94%)	B5, B6	07KNSTD
BE38788	RM-10-10	56.63592	-4.77492	316	130 x 125 x 98.75	0.66	1.000	14.9393	0.1809	1037	8.214 ± 0.19	6.86 ± 0.16	25.7 (95%)	B7	07KNSTD
BE38789	RM-10-11	56.63633	-4.77294	313	200 x 150 x 98.75	0.94	1.000	15.3106	0.1804	1037	8.389 ± 0.14	6.82 ± 0.11	29.6 (109%)	B7	07KNSTD
BE40327	RM-10-05	56.63385	-4.77544	324	280 x 150 x 50	1.60	1.000	11.1758	0.1837	1045	6.145 ± 0.15	7.03 ± 0.17	12.9 (49%)	B8	07KNSTD
BE40328	RM-10-09	56.63459	-4.78123	326	245 x 190 x 128.75	3.01	0.994	15.0141	0.1834	1045	7.830 ± 0.25	6.66 ± 0.22	21.8 (83%)	B8	07KNSTD
BE40329	RM-10-12	56.6352	-4.77243	316	190 x 130 x 77.5	1.93	1.000	10.8794	0.1825	1045	5.832 ± 0.13	6.81 ± 0.16	20.7 (79%)	B8	07KNSTD
BE40537	RM-10-04	56.63391	-4.77524	324	240 x 125 x 75	2.27	1.000	8.4336	0.1830	1046	4.888 ± 0.12	7.35 ± 0.18	24.7 (103%)	B9	07KNSTD
BE40538	RM-10-07	56.63407	-4.77674	325	155 x 130 x 55	1.41	1.000	10.6886	0.1834	1046	6.032 ± 0.15	7.19 ± 0.19	11.8 (49%)	B9	07KNSTD
BE40539	RM-10-08	56.63414	-4.77869	327	300 x 220 x 120	1.49	1.000	7.8106	0.1834	1046	4.340 ± 0.13	7.06 ± 0.21	20.5 (85%)	B9	07KNSTD

1058  
1059  
1060  
1061  
1062  
1063  
1064  
1065  
1066  
1067  
1068

<sup>a</sup> - Carrier concentrations have been corrected for evaporation.

<sup>b</sup> - Boron-corrected <sup>10</sup>Be/<sup>9</sup>Be. Ratios are not corrected for background <sup>10</sup>Be detected in procedural blanks.

<sup>c</sup> - Reported [<sup>10</sup>Be] values have been corrected for background <sup>10</sup>Be detected in procedural blanks.

<sup>d</sup> - <sup>9</sup>Be<sup>+</sup> measured after the accelerator. Reported currents are those measured during the first run of each sample. In parentheses is the ratio, given in percent, of each sample current compared with the average of all measured first-run AMS standard currents.

<sup>e</sup> - AMS standard to which respective ratios and concentrations are referenced. Reported <sup>10</sup>Be/<sup>9</sup>Be ratio for 07KNSTD is 2.85x10<sup>-12</sup>.

<sup>f</sup> - Procedural blanks used to correct sample concentrations. Blank numbers refer to those given in Table 2. Where two blanks are shown, the average (and propagated error) was used to correct sample concentrations in the respective sample batch.

1069 **Table 3.** Procedural blank <sup>10</sup>Be data.

Blank no.	CAMS laboratory no.	Sample ID	Corresponding samples	Carrier Added (g)	Carrier conc. (ppm) <sup>a</sup>	<sup>10</sup> Be/ <sup>9</sup> Be ± 1σ (10 <sup>-16</sup> ) <sup>b</sup>	N <sub>10Be</sub> ± 1σ (10 <sup>3</sup> atoms) <sup>c</sup>	<sup>9</sup> Be current (μA) <sup>d</sup>	AMS Std
1	BE34635	Blank_1_2012Dec07	RM-10-02, 03	0.1810	1030.34	1.057 ± 1.89	1.32 ± 2.35	16.0 (70%)	07KNSTD
2	BE34642	Blank_2_2012Dec21	RM-10-02, 03	0.1811	1030.34	3.437 ± 1.22	4.29 ± 1.52	18.9 (82%)	07KNSTD
3	BE35520	Blank_1_2013April15	RM-10-01	0.1833	1032	5.777 ± 1.10	7.30 ± 1.39	23.5 (88%)	07KNSTD
4	BE35522	Blank_2_2013April15	RM-10-01	0.1825	1032	9.516 ± 1.96	11.97 ± 2.47	20.7 (77%)	07KNSTD
5	BE38214	BLK1-2014Nov07	RM-10-06	0.1819	1036	0.450 ± 0.67	0.57 ± 0.84	25.6 (105%)	07KNSTD
6	BE38227	BLK2-2014Nov07	RM-10-06	0.1812	1036	2.343 ± 1.94	2.94 ± 2.43	24.8 (101%)	07KNSTD
7	BE38790	BLK2-2015Mar12	RM-10-10, 11	0.1814	1037	3.885 ± 1.05	4.88 ± 1.32	29.1 (107%)	07KNSTD
8	BE40326	BLK1-2015Dec10	RM-10-05, 09, 12	0.1835	1045	2.078 ± 1.06	2.66 ± 1.35	16.9 (64%)	07KNSTD
9	BE40548	BLK1-2016Jan11	RM-10-04, 07, 08	0.1835	1046	4.061 ± 1.32	5.21 ± 1.69	23.5 (98%)	07KNSTD

1070 a - Carrier concentrations have been corrected for evaporation.

1071 b - Boron-corrected <sup>10</sup>Be/<sup>9</sup>Be.

1072 c - Total <sup>10</sup>Be (in atoms) determined from each procedural blank.

1073 d - <sup>9</sup>Be<sup>+3</sup> measured after the accelerator. Reported currents are those measured during the first run of each sample. In parentheses is the ratio,  
1074 given in percent, of each sample current compared with the average of all measured first-run AMS standard currents.

1075 e - AMS standards to which respective ratios and concentrations are referenced. Reported <sup>10</sup>Be/<sup>9</sup>Be ratio for 07KNSTD is 2.85x10<sup>-12</sup>.

1070  
1071  
1072  
1073  
1074  
1075  
1076  
1077  
1078

1079 **Table 4.** Maximum-limiting, minimum-limiting, and midpoint  $^{10}\text{Be}$  production rates determined from the Rannoch Moor moraines  
 1080 ('PRM'), calculated with Version 3 of the UW online calculator using accepted scaling protocols. Recommended (i.e., midpoint)  
 1081 reference SLHL production-rate values/correction factors are given in bold.  $\chi^2$  values are given for 10 degrees of freedom (d.o.f).  
 1082 Expected  $\chi^2$  for 10 d.o.f. (evaluated at 95% confidence) = 18.31. 'St' and 'Lm' values are SLHL reference production rates, reported in  
 1083 units of [ $\text{at g}^{-1} \text{yr}^{-1}$ ]. As described in text, LSDn results are presented as non-dimensional correction factors (applicable to the output  
 1084 production rates from the Lifton et al. (2014) model).  
 1085

Scaling method	$P_{\text{RM}} \text{ MAX}$	$\chi^2$	$P_{\text{RM}} \text{ MIN}$	$\chi^2$	$P_{\text{RM}} \text{ MID}$	$\chi^2$
St	$<3.95 \pm 0.11$ (2.9%)	11.30	$>3.88 \pm 0.11$ (2.9%)	11.35	<b><math>3.91 \pm 0.11</math> (2.9%)</b>	11.07
Lm	$<3.95 \pm 0.11$ (2.9%)	11.30	$>3.89 \pm 0.11$ (2.9%)	11.35	<b><math>3.92 \pm 0.11</math> (2.9%)</b>	11.07
LSDn	$<0.787 \pm 0.023$ (2.9%)	11.38	$>0.773 \pm 0.022$ (2.9%)	11.42	<b><math>0.780 \pm 0.022</math> (2.9%)</b>	11.14

1086  
 1087  
 1088

1089 **Table 5a.** Maximum-limiting, minimum-limiting, and midpoint  $^{10}\text{Be}$  production rates determined from the Rannoch Moor moraines  
1090 ('P<sub>RM</sub>'), using accepted scaling protocols, compared to other SLHL reference production rates mentioned in text. As described in text,  
1091 LSDn results are presented as non-dimensional correction factors (applicable to the output production rates from the Lifton et al.  
1092 (2014) model. 'St' and 'Lm' values are SLHL reference production rates, reported in units of [at g<sup>-1</sup> yr<sup>-1</sup>]. 'GLOBAL' refers to the  
1093 primary global calibration data set of Borchers et al. (2016). 'BB' refers to the Baffin Bay calibration sites of Young et al. (2013).  
1094 'SWISS' refers to the data set of Claude et al. (2014) from the Chironico landslide deposit in southern Switzerland. 'NENA' refers to  
1095 the northeastern North American calibration data set of Balco et al. (2009). 'PERU1' refers to the calibration data set of Kelly et al.  
1096 (2015) from the tropical Peruvian Andes. 'PERU2' refers to the calibration data set of Martin et al. (2015) from the tropical Peruvian  
1097 Andes. 'NZ' refers to the Macaulay valley calibration site in the Southern Alps of New Zealand of Putnam et al. (2010). 'PAT' refers to  
1098 the Patagonian calibration sites of Kaplan et al. (2011). Uncertainties for single calibration were calculated by 'total scatter' in  
1099 Version 3 of the UW online calculator (SWISS, PERU1, PERU2, NZ). Uncertainties for calibrations containing multiple sites were  
1100 calculated by site-to-site' scatter (GLOBAL, BB, NENA, PAT). With the exception of the GLOBAL data set, all calibrations are  
1101 underpinned by absolute, site-specific  $^{14}\text{C}$  or U-Th dating control. Recommended (i.e., midpoint) reference production-rate  
1102 values/correction factors are given in bold.

Scaling method	P <sub>GLOBAL</sub>	P <sub>BB</sub>	P <sub>SWISS</sub>	P <sub>NENA</sub>	P <sub>PERU1</sub>	P <sub>PERU2</sub>	P <sub>NZ</sub>	P <sub>PAT</sub>	P <sub>RM</sub> MAX	P <sub>RM</sub> MIN	P <sub>RM</sub> MID
St	4.13 ± 0.16 (3.8%)	4.03 ± 0.015 (0.4%)	3.98 ± 0.13 (3.1%)	4.04 ± 0.26 (6.3%)	3.98 ± 0.21 (5.2%)	4.04 ± 0.26 (6.3%)	3.92 ± 0.06 (1.6%)	3.89 ± 0.07 (1.7%)	<3.95 ± 0.11 (2.9%)	>3.88 ± 0.11 (2.9%)	<b>3.91 ± 0.11 (2.9%)</b>
Lm	4.22 ± 0.11 (2.7%)	4.03 ± 0.015 (0.4%)	4.014 ± 0.13 (3.1%)	4.04 ± 0.25 (6.2%)	4.36 ± 0.23 (5.4%)	4.18 ± 0.26 (6.3%)	4.01 ± 0.06 (1.6%)	4.01 ± 0.06 (1.5%)	<3.95 ± 0.11 (2.9%)	>3.89 ± 0.11 (2.9%)	<b>3.92 ± 0.11 (2.9%)</b>
LSDn	0.846 ± 0.016 (1.9%)	0.776 ± 0.008 (1.1%)	0.836 ± 0.027 (3.2%)	0.856 ± 0.071 (8.3%)	0.835 ± 0.044 (5.3%)	0.852 ± 0.053 (6.3%)	0.847 ± 0.013 (1.6%)	0.835 ± 0.011 (1.4%)	<0.787 ± 0.023 (2.9%)	>0.773 ± 0.022 (2.9%)	<b>0.780 ± 0.022 (2.9%)</b>

1104  
1105  
1106

1107 **Table 5b.** Comparison of production rates given in Table 5a relative to the Rannoch Moor production rates from this study.

Scaling method	$P_{RM}/P_{GLOBAL}$	$P_{RM}/P_{BB}$	$P_{RM}/P_{SWISS}$	$P_{RM}/P_{NENA}$	$P_{RM}/P_{PERU1}$	$P_{RM}/P_{PERU2}$	$P_{RM}/P_{NZ}$	$P_{RM}/P_{PAT}$
St	0.95	0.97	0.98	0.97	0.98	0.97	1.00	1.01
Lm	0.93	0.97	0.98	0.97	0.90	0.94	0.98	0.98
LSDn	0.92	1.01	0.93	0.91	0.93	0.92	0.92	0.93

1108  
1109

1110 **Table 6a.** Production rates determined from previously published Scottish Highland sites mentioned in text, calculated using Version  
1111 3 of the UW online calculator with accepted scaling protocols. LSDn results are presented as non-dimensional correction factors  
1112 (applicable to the output production rates from the Lifton et al. (2014) model. 'St' and 'Lm' values are SLHL reference production  
1113 rates, reported in units of [at g<sup>-1</sup> yr<sup>-1</sup>]. The maximum, minimum, and midpoint <sup>10</sup>Be production rates from this study are provided for  
1114 reference. Recommended (i.e., midpoint) reference production-rate values/correction factors are given in bold. We removed one  
1115 anomalously high-concentration sample from the Coire nan Arr data set, and one anomalously low-concentration sample from the  
1116 Glen Roy data set. All calculations were conducted assuming zero erosion.

Scaling method	Coire nan Arr	$\chi^2$	Maol Chean Dearg	$\chi^2$	Coire Mhic Fearchair	$\chi^2$	Glen Roy	$\chi^2$	$P_{RM} MAX$	$\chi^2$	$P_{RM} MIN$	$\chi^2$	$P_{RM} MID$	$\chi^2$
St	4.21 ± 0.11 (2.6%)	14.96	4.17 ± 0.05 (1.2%)	0.77	4.23 ± 0.22 (5.1%)	4.85	4.24 ± 0.042 (1.0%)	0.07	<3.95 ± 0.11 (2.7%)	11.30	>3.88 ± 0.11 (2.7%)	11.35	<b>3.91 ± 0.11 (2.7%)</b>	11.07
Lm	4.21 ± 0.11 (2.6%)	14.95	4.18 ± 0.05 (1.2%)	0.77	4.24 ± 0.22 (5.2%)	4.87	4.24 ± 0.042 (1.0%)	0.07	<3.95 ± 0.11 (2.7%)	11.30	>3.89 ± 0.11 (2.7%)	11.35	<b>3.92 ± 0.11 (2.7%)</b>	11.07
LSDn	0.829 ± 0.022 (2.6%)	14.84	0.831 ± 0.01 (1.2%)	0.77	0.844 ± 0.044 (5.2%)	4.97	0.845 ± 0.008 (1.0%)	0.07	<0.787 ± 0.021 (2.7%)	11.38	>0.773 ± 0.021 (2.7%)	11.42	<b>0.780 ± 0.021 (2.7%)</b>	11.14

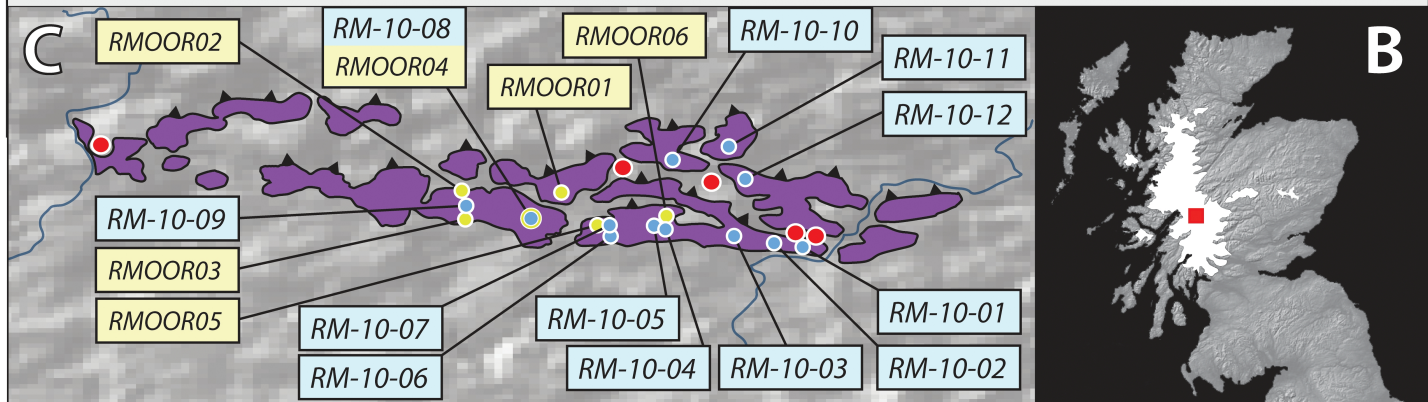
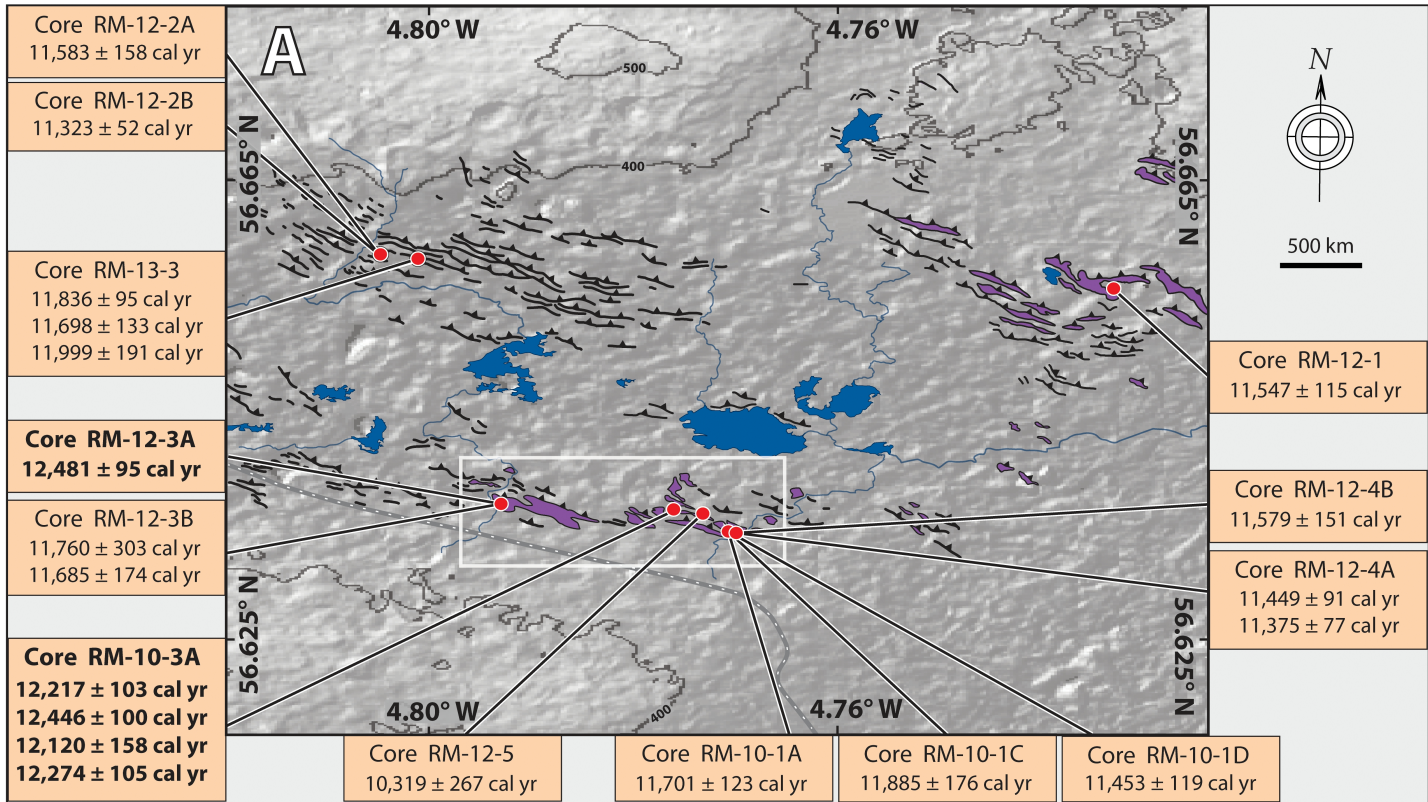
1117  
1118  
1119

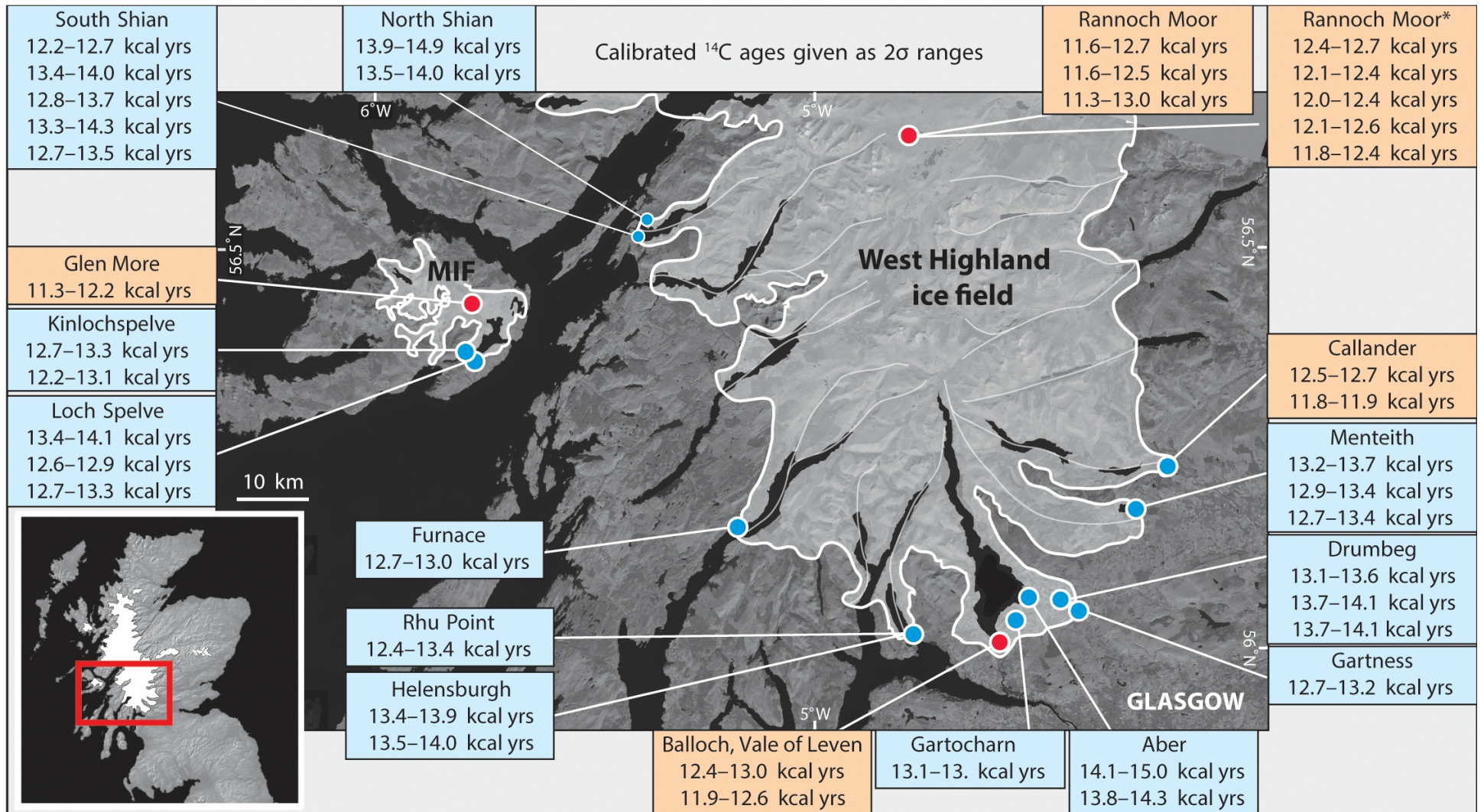
1120 **Table 6b.** Comparison of published Scottish production rates (Table 6a) relative to the Rannoch Moor production rates from this  
1121 study. Abbreviations: 'RM' is Rannoch Moor; 'CnC' is Coire nan Arr; 'MCD' is Maol Chean Dearg; 'CMF' is Coire Mhic Fearchair; 'GR' is  
1122 Glen Roy.

1123

Scaling method	$P_{RM}/P_{CnC}$	$P_{RM}/P_{MCD}$	$P_{RM}/P_{CMF}$	$P_{RM}/P_{GR}$	$P_{RM}$ maximum limit			
		$(P_{RM} \text{ midpoint})$			$P_{RM}/P_{CnC}$	$P_{RM}/P_{MCD}$	$P_{RM}/P_{CMF}$	$P_{RM}/P_{GR}$
St	0.93	0.94	0.92	0.92	0.94	0.95	0.93	0.93
Lm	0.93	0.94	0.92	0.92	0.94	0.94	0.93	0.93
LSDn	0.94	0.94	0.92	0.92	0.95	0.95	0.93	0.94

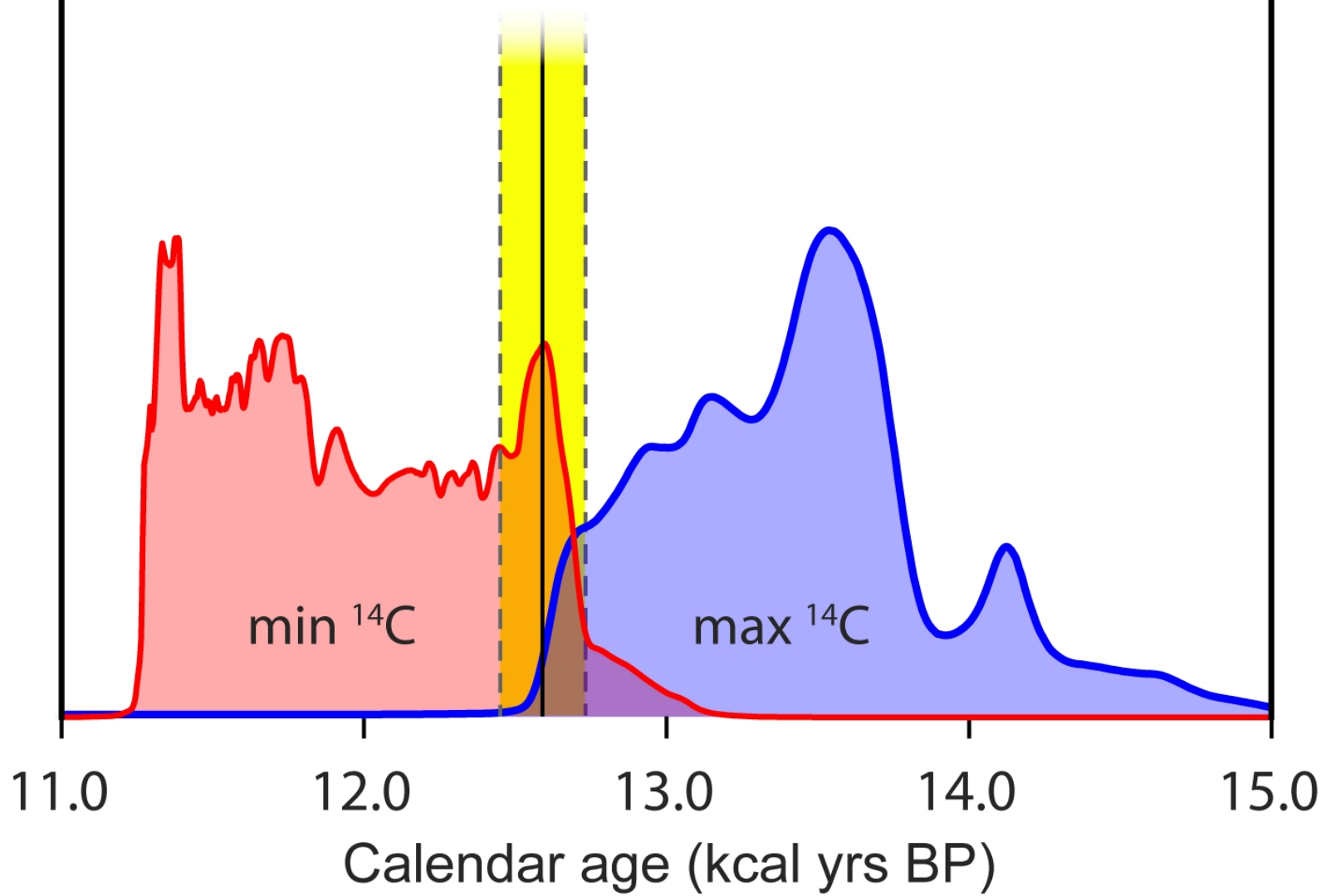
1124







Midpoint age of Rannoch Moor moraine belt;  
 $12,590 \pm 140$  cal yrs BP



a) RM-10-02



b) RM-10-05



c) RM-10-06



d) RM-10-08  
(RMOOR04)



e) RM-10-11



f) RM-10-12



